



# 1 Improving Antarctic Bottom Water precursors in NEMO for climate 2 applications

3 Katherine Hutchinson <sup>1</sup>, Julie Deshayes <sup>1</sup>, Christian Éthé <sup>1</sup>, Clément Rousset <sup>1</sup>, Casimir de Lavergne <sup>1</sup>,  
4 Martin Vancoppenolle <sup>1</sup>, Nicolas C. Jourdain <sup>2</sup>, and Pierre Mathiot <sup>2</sup>

5  
6 <sup>1</sup> LOCEAN Laboratory, Sorbonne Université CNRS-IRD-MNHN, Paris, France

7 <sup>2</sup> Univ. Grenoble Alpes/CNRS/IRD/G-INP, IGE, Grenoble, France

8 *Correspondence to:* Katherine Hutchinson (kath.hutchinson@gmail.com)

9 **Abstract.** The world's largest ice shelves are found in the Antarctic Weddell and Ross Seas where complex interactions  
10 between the atmosphere, sea ice, ice shelves and ocean transform shelf waters into High Salinity Shelf Water (HSSW) and Ice  
11 Shelf Water (ISW), the parent waters of Antarctic Bottom Water (AABW). This process feeds the lower limb of the global  
12 overturning circulation as AABW, the world's densest and deepest water-mass, spreads outwards from Antarctica. None of  
13 the coupled climate models contributing to CMIP6 directly simulated ocean-ice shelf interactions, thereby omitting a  
14 potentially critical piece of the climate puzzle. As a first step towards better representing these processes in a global ocean  
15 model, we run a 1° resolution forced configuration of NEMO (eORCA1) to explicitly simulate circulation beneath Filchner-  
16 Ronne (FRIS), Larsen C (LCIS), and Ross (RIS) ice shelves. These locations are thought to supply the majority of the source  
17 waters for AABW and so melt in all other cavities is provisionally prescribed. Results show that the grid resolution of 1° is  
18 sufficient to produce melt rate patterns and net melt rates of FRIS ( $117 \pm 21$  Gt/yr), LCIS ( $36 +7$  Gt/yr) and RIS ( $112 + 22$   
19 Gt/yr) that agree well with both high resolution models and satellite measurements. Most notably, allowing sub-ice shelf  
20 circulation reduces salinity biases (0.1 psu), produces the previously unresolved water mass ISW, and re-organises the shelf  
21 circulation to bring the regional model hydrography closer to observations. A change in AABW within the Weddell and Ross  
22 Seas towards colder, fresher values is identified but the magnitude is limited by the absence of a realistic overflow. This study  
23 presents a NEMO configuration that can be used for climate applications with improved realism of the Antarctic continental  
24 shelf circulation and a better representation of the precursors of AABW.

25  
26 **Plain language summary.** Bottom Water constitutes the lower limb of the ocean's overturning system and is primarily  
27 formed in the Antarctic Weddell and Ross Seas due to interactions between the atmosphere, ocean, sea ice and ice shelves.  
28 Here we use a global ocean 1° resolution model with the three large ice shelves important for the formation of the parent  
29 waters of Bottom Water explicitly represented and find doing so reduces salinity biases, improves water mass realism, and  
30 gives realistic ice shelf melt rates.



## 31 **1 Introduction**

32 The Southern Ocean plays a vital role in global ocean circulation and in the storage of both heat and carbon (Marshall and  
33 Speer, 2012; Rintoul, 2018). Within this backdrop, the processes taking place adjacent to and underneath the Antarctic ice  
34 shelves are not only important for controlling regional ocean dynamics but also for facilitating globally important water mass  
35 transformations (Schodlok et al., 2015). Sea ice formation on the continental shelf decreases the buoyancy of the underlying  
36 waters through the process of brine rejection creating High Salinity Shelf Water (HSSW). When this dense water mass is  
37 formed adjacent to an ice shelf, it can follow deep bathymetric pathways into the neighboring sub-ice shelf cavity and  
38 interact with the base of the ice to form Ice Shelf Water (ISW). These dense waters then accumulate on the continental shelf  
39 and migrate towards the shelf break to cascade down the continental slope as a gravity current (Gordon, 1986; Whitehead,  
40 1987). As the waters descend towards the depths, they mix with and entrain ambient water masses until they reach either a  
41 density neutral depth, or the sea floor, at which point they spread outwards as Antarctic Bottom Water (AABW)  
42 (Bergamasco et al., 2003; Huthnance 1995). AABW plays a crucial role in the global overturning circulation, in abyssal  
43 ventilation and in the cross-basin transport of heat, salt, carbon, nutrients and numerous other tracers (Killworth, 1983;  
44 Johnson, 2008; Orsi, 2010). The principal locations for the formation of the source waters of AABW are the Weddell and  
45 Ross Seas adjacent to the large ice shelves (Orsi et al., 1999; van Caspel et al., 2015; Kerr et al., 2018; Bowen et al., 2021).

46  
47 Filchner Ronne Ice Shelf (FRIS) is located at the southern boundary of the Weddell Sea and represents 28% of the total  
48 Antarctic ice shelf area (Fig. 1b). Traditionally FRIS has been viewed as having the greatest contribution to AABW by  
49 forming the coldest and most oxygen-rich dense waters in the Southern Ocean (Nicholls et al., 2009; Naveira Garabato et al.,  
50 2002). Observations for the southern Weddell Sea continental shelf indicate that HSSW enters the FRIS cavity following the  
51 Ronne Depression (Fig. 1b), circulates under the cavity causing melting at the base of the ice shelf at great water pressures  
52 and then exits as colder and fresher ISW via the Filchner Trough (Nicholls et al., 2001; Nicholls et al., 2004; Janout et al.,  
53 2021). This outflowing ISW mixes with HSSW formed on the shallow continental shelf adjacent to Berkner Island and  
54 cascades down the continental slope, mixing with ambient modified Circumpolar Deep Water (CDW) to form AABW  
55 (Fahrback et al., 1995; Nicholls et al., 2009).

56  
57 While the main formation site of the source waters of AABW in the Weddell Sea is the FRIS continental shelf, Larsen-C Ice  
58 Shelf (LCIS) is also thought to play an important role. Nestled into the arc of the Antarctic Peninsula (Fig. 1b), processes  
59 adjacent to this ice shelf produce a fresher variety of dense water called Weddell Sea Deep Water (WSDW), which is lighter  
60 than the Weddell Sea Bottom Water (WSBW) formed further south (Fahrback et al., 1995; Gordon et al., 2001). This water  
61 mass is less hindered by bathymetric constraints so that it is more easily transported out of the gyre over the South Scotia  
62 Ridge to make a valuable contribution to AABW (Abrahamsen et al., 2019; van Caspel et al., 2015).

63  
64 The Ross Sea, the second largest site for AABW formation, is home to Antarctica's largest ice shelf representing 32 % of the  
65 total Antarctic ice shelf area (Rignot et al., 2013). The Ross Ice Shelf (RIS) is located at the southern boundary of the Ross  
66 Sea (Fig. 1a) where the continental shelf has very irregular topography with numerous troughs and depressions that act as  
67 reservoirs for dense waters (Budillon et al., 2003). Just offshore, CDW flows largely un-modified within the Ross Gyre and  
68 mixes with the local waters at the shelf break (Fig. 1a), providing a source of heat and making this a region of dynamic water  
69 mass exchange (Bergamasco et al., 2003; Budillon et al., 2003). Two recurring ice-free zones are the principal formation  
70 sites for HSSW in the area: one located at the south-western corner of the Ross Sea called the Terra Nova Bay polynya and  
71 another in front of RIS called the Ross Sea Polynya. This HSSW then spreads both northwards towards the shelf break and  
72 southwards under RIS (Fig. 1a). Similarly to FRIS, the HSSW flowing into the RIS cavity interacts with the base of the ice  
73 shelf to form ISW (Jacobs et al., 1979).



74  
75 While freshwater input to the ocean from ice shelf melt is (at present) relatively small in magnitude, it exerts a strong  
76 modulating effect on dense water formation and Southern Ocean water mass transformation (Schodlok et al., 2015; Jeong et  
77 al., 2020). The impacts of increased meltwater in a warming climate could, in addition to raising sea level, actually reduce  
78 AABW formation with major consequences for global overturning (Silvano et al., 2018). One possible series of events  
79 common to simulations by the E3SM, CSIRO Mk3L and LOVECLIM climate models describes how surface freshening  
80 from ice shelf melt would increase stratification along the Antarctic coast, inhibit full depth convection and the formation of  
81 dense shelf water, and simultaneously trap warm water at depth resulting in further ice shelf melting and a horizontal  
82 propagation of the warming signal (Jeong et al., 2020; Phipps et al., 2016; Menviel et al., 2010).

83  
84 Despite the importance of ocean-ice shelf interactions for the climate system, none of the models contributing to the DECK  
85 experiments of the Coupled Model Intercomparison Project Phase 6 (CMIP6, used to inform the Intergovernmental Panel on  
86 Climate Change (IPCC) assessment report 6 (AR6)) explicitly represented circulation within sub-ice shelf cavities (Heuze et  
87 al., 2021). This has lowered confidence in projected trends for the Southern Ocean and has limited our ability to incorporate  
88 the impacts of global ocean warming on the Antarctic Ice Sheet (Meredith et al., 2019; Beadling et al., 2020; Comeau et al.,  
89 2022). In most coupled climate models, the formation of dense water is poorly represented as AABW is formed via open  
90 ocean convection, often with mixed layers that are too deep, and polynyas that are too large and too frequent (Heuze et al.,  
91 2013; Mohrmann et al., 2021). In reality, deep open-ocean convection events able to produce AABW are rarely observed  
92 (Goosse et al. 2021) and instead ocean–sea-ice–atmosphere interactions adjacent to the Antarctic ice shelves are responsible  
93 for the creation of the majority of AABW source waters.

94  
95 The authors propose that the path towards improving AABW realism in coupled climate models starts with a more accurate  
96 simulation of the dense precursors on the Antarctic continental shelf. Then work needs to be done on improving the  
97 overflows so as to facilitate the downslope export of these waters, and on decreasing the strength of open ocean convection  
98 (Heuze et al., 2021). The Nucleus for European Modelling of the Ocean (NEMO) model is used as the ocean component in  
99 many climate models (Hazeleger et al., 2010; Scoccimarro et al., 2011; Hewitt et al., 2011, 2016; Dufresne et al., 2013;  
100 Voltaire et al., 2013; Cao et al., 2018; Swart et al., 2019) and consequently the development of configurations with  
101 improved realism of Antarctic shelf water circulation and AABW source water properties is of interest to a large community.

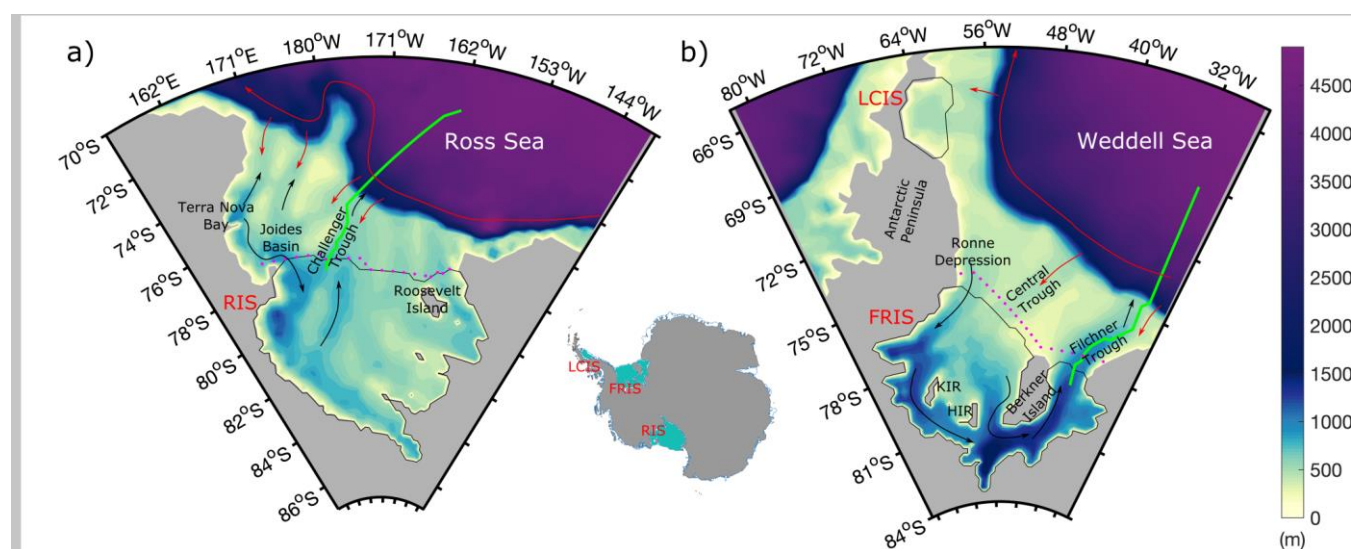
102  
103 Ice shelf melt has previously been represented using NEMO in a variety of ways: prescribed using a freshwater flux at the  
104 surface, a fixed flux distributed over the depth range of the mouth of the ice shelf front, a specified melt at the base of the ice  
105 shelf, and an interactive melt with both fixed geometry and evolving coupled ice shelves (Mathiot et al., 2017; Storkey et al.,  
106 2018; Smith et al., 2021). The simulations with a fixed freshwater flux parameterisation at depth perform well in terms of  
107 mimicking the vertical overturning and associated entrainment of ice shelf melt. This representation, however, is limited by  
108 its inability to produce the horizontal variability observed adjacent to large ice shelves and it does not allow for interactive  
109 ice-ocean exchange that evolves with ocean properties. For this, it is necessary to allow for circulation underneath the ice  
110 shelf (Mathiot et al., 2017; Storkey et al., 2018; Comeau et al., 2022). Of all the previous studies using NEMO  
111 configurations with explicit sub-ice shelf cavities, only one has been at a resolution that is compatible with long-term climate  
112 projection applications, that developed by Smith et al. (2021) where a global ocean 1° NEMO (eORCA1) is coupled with  
113 interactive ice sheets in the the U.K. Earth System model (UKESM). Previous studies have proven very useful in illustrating  
114 the strengths and weaknesses of NEMO’s representation of ocean-ice shelf interactions but the results apply to regional  
115 configurations (e.g. Mathiot et al., 2017; Jourdain et al., 2017; Hausmann et al., 2020; Huot et al. 2021) or high resolution  
116 global configurations (e.g. 1/4° and 1/12° in Storkey et al., 2018) and so do not fit the needs of typical CMIP models. The  
117 results presented by Smith et al. (2021) for UKESM with NEMO eORCA1 coupled to an Antarctic ice sheet model highlight



118 the substantial advancement in model development, but do not show how this coupling affects the realism of Southern Ocean  
119 water mass properties and dynamics. Evaluation of the initial state of the UKESM (NEMO coupled to BICYCLES ice sheet  
120 model) was undertaken by Siahaan et al. (2021), but the investigation served to check for the absence of large biases and so  
121 an in-depth comparison was not carried out.

122  
123 A gap therefore exists to take a step-by-step approach to represent ice shelf-ocean interactions in NEMO for climate  
124 applications. Additionally, a well documented description of one possible method to simulate sub-ice shelf cavity circulation  
125 in low resolution ocean models could be of use in the designing of the next phase of CMIP. In this study we present the first  
126 proposed step in this journey by explicitly simulating circulation under only Ross Ice Shelf (RIS), Filchner-Ronne Ice Shelf  
127 (FRIS) and Larsen C Ice Shelf (LCIS). We choose to keep all other ice shelves closed with prescribed melt rates injected at  
128 the mouth of the front using the method described by Mathiot et al. (2017). RIS, FRIS and LCIS were chosen due to their  
129 role in the formation and setting of properties of the parent waters of AABW (Kerr et al., 2018; Bowen et al., 2021), and due  
130 to their large size and thus practicality of realistically simulating their sub-ice shelf cavities in a global ocean 1° setup. We  
131 choose to explore the changes in circulation, melt rates, and water mass properties in a forced scenario with fixed cavity  
132 geometry as coupling can introduce further biases and obscure the changes attributed to sub-ice shelf circulation. By taking  
133 this circumspect approach it is possible to diagnose the impact of ocean-ice shelf interactions on the parent waters of AABW  
134 and produce a validated configuration of NEMO that can either be used for the next generation of climate models or as an  
135 interim step towards dynamic ice-sheet coupling.

136  
137 The model setup, configurations used in this study, forcing, and methodology to establish initial conditions under the ice  
138 shelves are described in Sect. 2. A validation of the reference configuration compared to ocean observations is presented in  
139 Sect. 3. Sect. 4 then explores the results from the “Open” cavity simulation and compares melt rates and thermohaline  
140 properties with other model estimates and observed values. Sect. 5 provides the reader with a discussion and Sect. 6 presents  
141 a conclusion of the findings of this study. Additional information regarding sea ice, volume and density changes along with  
142 an analysis of mixed layer depths in the model compared to an observational atlas are provided in Supplementary Material.  
143



144  
145 Figure 1: Model bathymetry for (a) the Ross and (b) Weddell Seas with main topographic features labeled (KIR: Korff Ice  
146 Rise; HIR: Henry Ice Rise). Red arrows show direction of flow of warm deep water and black arrows indicate dense shelf



147 water circulation according to observational estimates. Circulation features depicted in this figure are adapted from  
148 information presented in Budillon et al. (2003), Bergamasco et al. (2003), Russo et al. (2011) and Janout et al. (2018).  
149 Magenta dotted lines indicate sections used for CTD comparisons and green lines show shelf cross sections used for analysis  
150 in Figs. 8 and 9.

## 151 **2 Methods**

### 152 **2.1 Model setup**

153 For this study version 4.2 of NEMO is used (NEMO System Team, 2022). NEMO is a three-dimensional, free-surface,  
154 hydrostatic, primitive-equation global ocean general circulation model. Our configuration uses the eORCA1 global grid with  
155 nominal horizontal resolution of  $1^\circ$  at the equator and a reduction in meridional grid spacing towards higher latitudes to  
156 match the accompanying shrinking of the zonal dimension of the grid cells. In the Southern Hemisphere, the model grid has  
157 been extended to reach  $85^\circ$  S to allow for the representation of the sub-ice shelf seas according to the procedure described in  
158 Mathiot et al. (2017). The average horizontal resolution of the grid under RIS, FRIS, and LCIS is 20 km, 22 km and 42 km  
159 respectively. To account for the decrease in the horizontal size of grid cells at high latitudes, we decide to scale horizontal  
160 eddy viscosity south of  $65^\circ$  S according to grid cell size. In the vertical, the configuration possesses 75 levels, with thickness  
161 increasing from 1 m at the surface to 200 m at depth (Storkey et al., 2017). We use the  $z^*$  vertical coordinate adapted to the  
162 ice shelf so that all cells between the surface and the ice shelf base are masked at initialisation and the effect of the ice shelf  
163 on friction and pressure gradient is calculated (Madec and NEMO team, 2016; Mathiot et al., 2017). The bathymetry used is  
164 derived from the ETOPO2v2 data set (NOAA, 2006) with information for the extension under the ice shelves based on  
165 IBSCO (Arndt et al., 2013). For the calculation of the thermodynamic properties of seawater, NEMO uses TEOS-10 giving  
166 results in conservative temperature and absolute salinity which for the purposes of this study were converted to potential  
167 temperature and practical salinity in order to facilitate comparison of the model results with observations and known  
168 signatures of water masses. For more information regarding the choices of advection and diffusion schemes, mixing  
169 coefficients, and eddy parameterizations, please refer to the copy of the namelists provided in the accompanying data  
170 repository.

171  
172 The ocean dynamics component, NEMO OCE, is coupled with SI<sup>3</sup>, the dynamic and thermodynamic sea ice model of  
173 NEMO (Rousset et al., 2015; Vancoppenolle et al., 2023). SI<sup>3</sup> is directly resolved on the ocean grid, based on an energy- and  
174 salt- conserving approach for sea ice thermodynamics (Vancoppenolle et al., 2009), multiple categories to resolve subgrid  
175 scale variations in ice thickness (Bitz et al., 2001; Lipscomb, 2001), a second-order moment-conserving scheme for  
176 horizontal advection (Prather, 1986), and the adaptive elastic-viscous-plastic formulation for the rheology term of the  
177 momentum equation (Kimmritz et al., 2016).

### 178 179 **2.2 Open vs Closed Configurations**

180  
181 Results from two configurations are presented here: first a “Closed” cavity reference configuration where ice shelf melt is  
182 prescribed in a way to mimic the ice-shelf overturning, and secondly an “Open” cavity configuration. For the reference  
183 “Closed” cavity configuration, a fixed freshwater flux corresponding to the volume of basal meltwater estimated by  
184 Depoorter et al. (2013) for each ice shelf is added into the ocean evenly between the ocean floor and the base of the ice shelf  
185 at the location of the ice shelf front and a vertical wall closes the cavity at this location (as in Mathiot et al., 2017). For the  
186 “Open” cavity configuration, the majority of ice shelves are kept closed using the same method as described above and only  
187 three of the largest cold-core ice shelves are opened. Circulation is simulated under RIS, FRIS and LCIS where the



188 prescribed freshwater flux is turned off at the mouths of these cavities and interactive melt is activated. Ice shelf melt and  
189 freeze are calculated using the 3-equation formulation (Hellmer and Olbers, 1989; Holland and Jenkins, 1999; Asay-Davis et  
190 al., 2016) in which the temperature, salinity and velocities are averaged over a fixed boundary layer thickness of 30m  
191 (Losch, 2008). The top drag coefficient used is  $10^{-3}$  and the temperature and salinity transfer coefficients used are  $1.4 \times 10^{-2}$   
192 and  $4 \times 10^{-4}$  respectively. Note that a fixed ice shelf geometry is maintained, thereby assuming a steady-state where all ice  
193 melted by the ocean is replaced by the seaward advection of new ice (Schodlok et al., 2015; Mathiot et al., 2017).

194  
195 By using this combination of explicit and parameterised ice shelf cavities, we provide an intermediate step between  
196 prescribed melt and explicit cavities or even ice sheet coupling, and gain experience and a better understanding of the impact  
197 on ocean dynamics in order to better inform future choices. The advantage of this approach is that it allows us to specify the  
198 melt for small cavities which remain unresolved or insufficiently resolved at a  $1^\circ$  resolution, and simultaneously utilize the  
199 model capability to resolve sub-ice shelf cavity circulation under the large cold ice shelves, which allows for more realistic  
200 formation of the source waters of AABW. Figure 1 shows the extended bathymetry of eORCA1 for the Weddell and Ross  
201 seas with the three ice shelf cavities of interest un-masked and important features labeled.

### 202 203 **2.3 Forcing**

204  
205 For both “Open” and “Closed” configurations, the model was run for 124 years using 2 cycles of interannual (1948-2009)  
206 CORE forcing (Coordinated Ocean - ice Reference Experiments; Large & Yeager, 2004; Griffies et al., 2009). Sea surface  
207 salinity restoring is activated, but not under sea ice as we have low confidence in the sea surface salinity climatology in this  
208 area due to limited observations. Freshwater discharge from iceberg melt is parameterized using a prescribed surface flux  
209 (Merino et al., 2016) based on calving estimates from Depoorter et al. (2013).

### 210 211 **2.4 Initial conditions**

212  
213 For all simulations, global ocean properties were initialized using the 1981-2010 climatology of World Ocean Atlas 2013  
214 (WOA2013; Locarnini et al., 2013; Zweng et al., 2013). This climatology does not, however, extend under the Antarctic ice  
215 shelves and so in order to provide somewhat realistic initial conditions underneath FRIS, LCIS, and RIS, we employed an  
216 idealized regional configuration of each ice shelf. For this we created a NEMO test case using a closed domain, with  
217 temperature and salinity restoring at the boundaries, 75 vertical layers and a resolution, timestep and bathymetry  
218 corresponding to that of eORCA1. The domain for each of the 3 configurations included just the ice shelf and adjacent  
219 continental shelf and slope and so were reasonably low-cost and fast to run in order to perform sensitivity experiments. The  
220 simulations were initialized with a constant and uniform temperature and salinity and restored at the boundaries using a  
221 mean profile from WOA2013 for that region. The choices for initial thermohaline properties inside the cavities were  
222 informed by calculating the mean properties of detected ISW from CTD observations performed in the area adjacent to each  
223 ice shelf and converting these to conservative temperature and absolute salinity for input to the model ( $-2^\circ\text{C}$  and 34.76 for  
224 FRIS (Janout et al., 2021),  $-1.95^\circ\text{C}$  and 34.74 for LCIS (Nicholls et al., 2004; Hutchinson et al., 2020), and  $-1.94^\circ\text{C}$  and  
225 34.76 for RIS (Bergamasco et al., 2003; Budillon et al., 2003). Each simulation was run for 10 years, which was found to be  
226 sufficiently long to spin-up the circulation within each cavity and reach a stable melt rate. The temperature-salinity  
227 distributions within the cavity were extracted and merged with WOA data re-gridded to the NEMO eORCA1 grid, with a  
228 cubic spline used to smooth the data discontinuity across the ice shelf front. By following this method we have attempted to  
229 provide as realistic initial conditions for eORCA1 as possible with the simulation starting with CORE forcing from the 1st of  
230 January 1948.



232 **3 Water mass realism in NEMO without cavities**

233

234 To assess the existing biases in the representation of dense water properties in NEMO v4.2 eORCA1 standard configuration  
235 (“Closed”), full depth temperature versus salinity plots along with bottom temperature and salinity are compared with World  
236 Ocean Atlas (WOA 2018) gridded observations from 1981-2010 (Locarnini et al., 2018; Zweng et al., 2019) in Figs. 2 and 3  
237 for the Weddell and Ross Seas respectively.

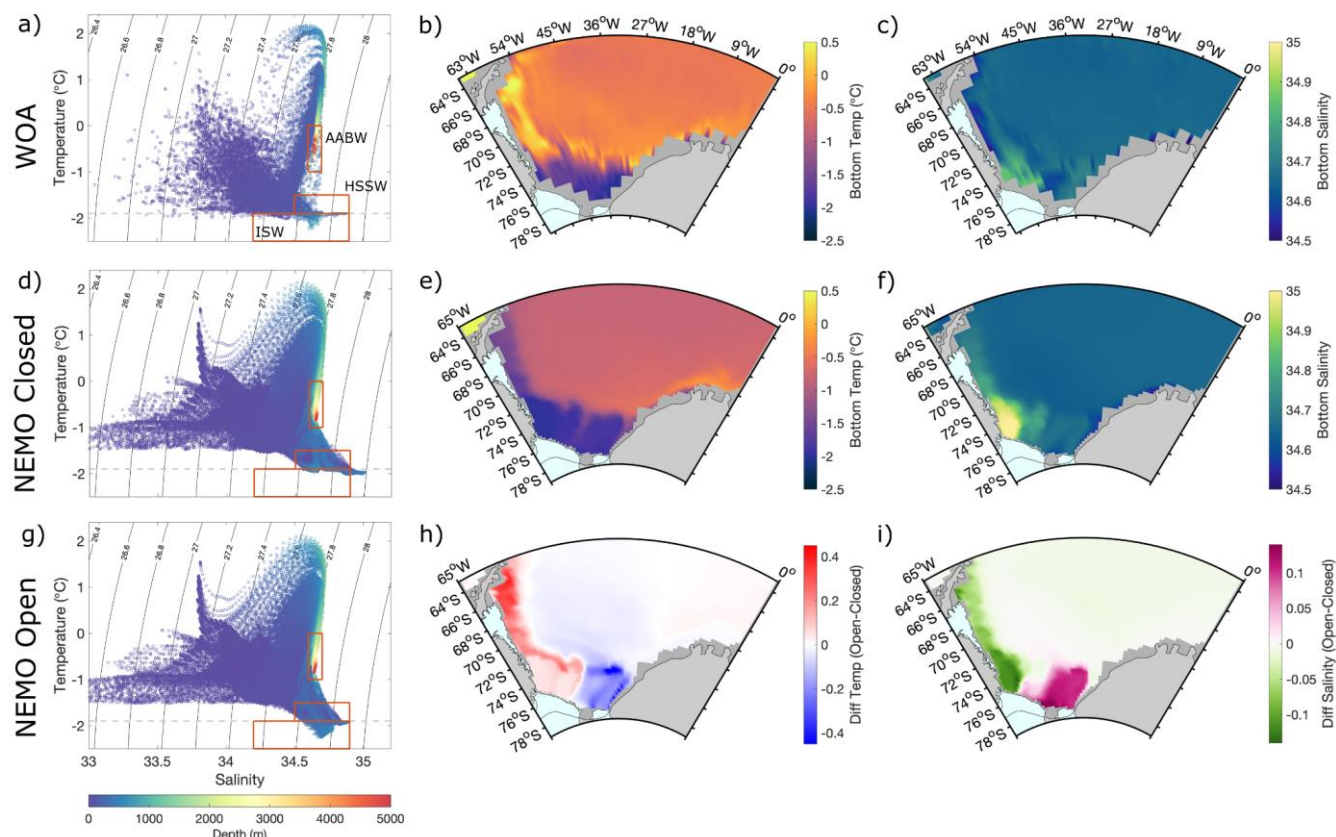
238

239 WOA observations indicate the presence of HSSW on the south-western continental shelf of the Weddell Sea, possessing  
240 salinities of up to 34.9 psu, likely sourced from the coastal polynya along the western flank of FRIS ice shelf front (Figs. 2a,  
241 2c and Supplementary Fig. S3a). On the eastern side of the FRIS ice shelf front, evidence of ISW can be seen with  
242 temperatures below surface freezing point ( $-1.9\text{ }^{\circ}\text{C}$ ) and fresher salinities of around 34.65 psu (Figs. 2a and 2b). Results from  
243 CTD observations obtained on the continental shelf in front of FRIS propose a counter-clockwise circulation pattern with  
244 HSSW entering the cavity via the Ronne Depression and ISW exiting via the Filchner Trough (Fig. 1b; Janout et al., 2021).  
245 By comparison, the standard model configuration is overall too salty on the continental shelf with HSSW properties that are  
246 out of the bounds of the observed range (HSSW box Fig. 2d). Most notably, there is a pool of HSSW that has built up in the  
247 Ronne Depression resulting in overestimations of bottom salinity and exaggerated cool conditions on the southwestern  
248 Weddell shelf (Figs. 2e and 2f). In terms of ISW, there is none detected in the model output (ISW box Fig. 2d) as in this  
249 configuration there is no explicit ocean-ice shelf interaction. Offshore bottom temperature is overall colder than in WOA,  
250 resulting in a core AABW signature that is at the lower limit of observed values (Fig. 2d). This is indicative of the effects of  
251 strong open ocean deep convection (Heuze et al., 2021) which is highlighted in Supplementary Fig. S2c by the over-deep  
252 mixed layers in the central Weddell Gyre.

253

254 Due to the limited observations adjacent to LCIS, WOA bottom properties do not capture the cold water masses located on  
255 the continental shelf detected by Hutchinson et al. (2020), where bottom temperatures of below  $-2\text{ }^{\circ}\text{C}$  and salinities of 34.6  
256 psu were reported. Instead Fig. 2b indicates very warm conditions (temperatures of around  $0.5\text{ }^{\circ}\text{C}$ ) on the western flank of the  
257 Weddell Sea. The authors explored the bottom properties in this area in the Southern Ocean State Estimate (SOSE; Mazloff  
258 et al., 2010) atlas and found bottom temperatures on the shelf adjacent to LCIS in line with those reported from hydrographic  
259 observations ( $-2\text{ }^{\circ}\text{C}$ ) but the bottom salinities were found to be far too fresh (34.5 psu). A fair comparison can therefore not  
260 be realistically made between NEMO and an atlas for the area adjacent to LCIS but by comparing the model output with the  
261 CTD results from Hutchinson et al. (2020; Fig. 3b) we find the “Closed” configuration to be too saline with bottom salinities  
262 (34.8 psu) greater than that observed. The overly saline conditions along the western flank of the Weddell Sea are likely a  
263 spill-over effect from the HSSW buildup seen in the Ronne Depression further south (Fig. 2f).

264



265  
 266

267 Figure 2: Weddell Sea comparison of NEMO v4.2 eORCA1 reference configuration (“Closed”; subplots d-f) for equivalent  
 268 years 1981-2009 to be compared with World Ocean Atlas (WOA; Locarnini et al., 2018; Zweng et al., 2018) observational  
 269 dataset (subplots a-c). The temperature salinity-distributions in density space are shown in plots (a), (d) and (g) with the  
 270 dashed gray line representing surface freezing point and labels in plot (a) indicating the observed ranges for properties  
 271 corresponding to Antarctic Bottom Water (AABW), High Salinity Shelf Water (HSSW) and Ice Shelf Water (ISW)  
 272 (Robertson et al., 2002; Hutchinson et al., 2020). Plots (b), (c), (e) and (f) show bottom temperature and salinity, and the  
 273 difference in bottom properties between the “Open” and “Closed” cavity configurations (Open - Closed) are shown in  
 274 subplots (h) and (i).

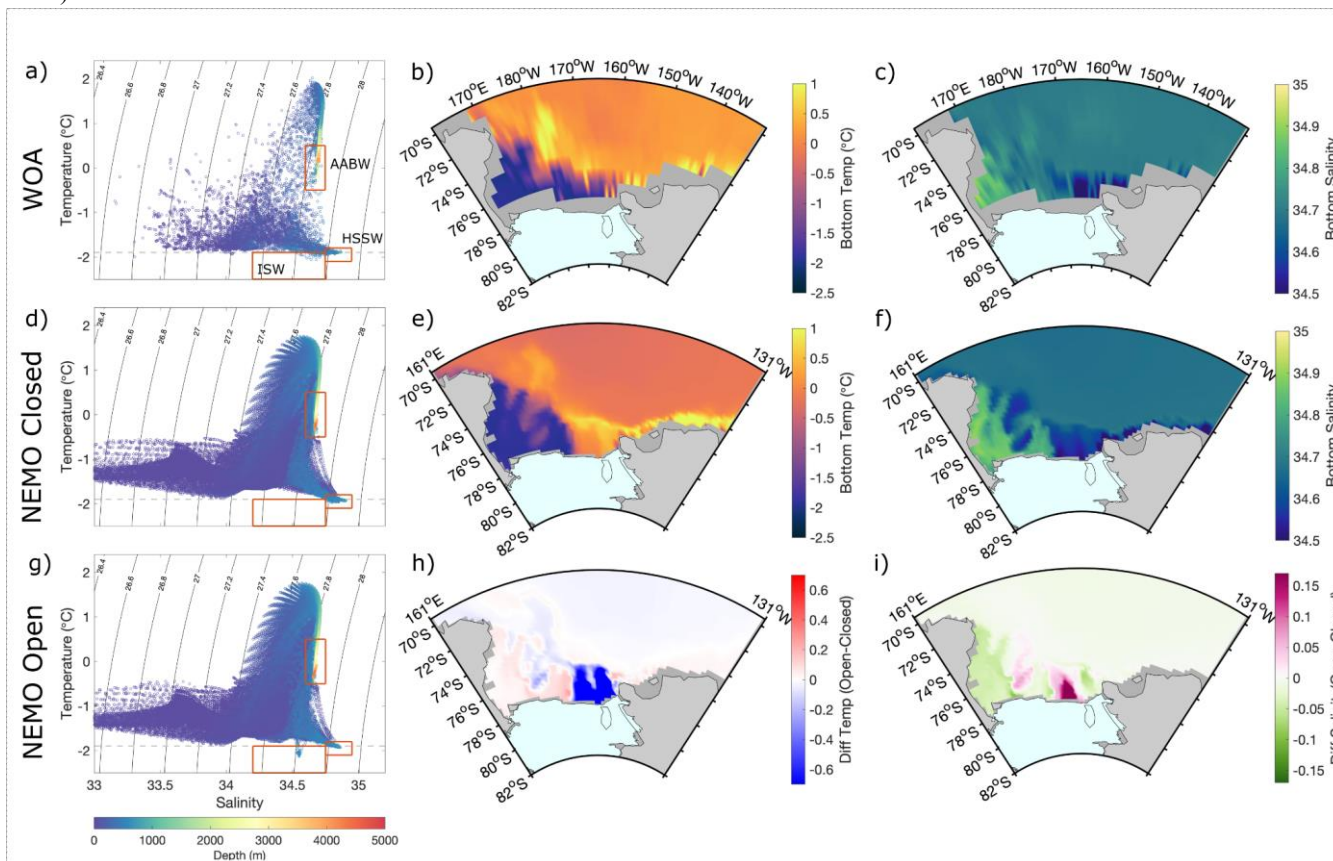
275

276 WOA bottom temperature and salinities for the Ross Sea indicate a strong east-west gradient in properties across the  
 277 continental shelf (Figs. 3b and 3c). Conditions in the south west reveal the cold and salty signature of HSSW likely formed  
 278 in the Terra Nova Bay polynya and the Ross Polynya. Intrusions of CDW at the eastern portion of the RIS front can be seen  
 279 by warm signatures of up to 1 °C (Figs. 3a and 3b) and fresher bottom salinities (Fig. 3c). Hydrological and current meter  
 280 data presented by Budillon et al. (2011) reported that HSSW dominates bottom properties within the troughs connected to  
 281 the Joides Basin, and ISW dominates in the Challenger Trough (see locations of bathymetric features in Fig. 1a) thus  
 282 indicating a western intensified anticlockwise circulation cell under RIS. In terms of HSSW properties, the model is within  
 283 the observed range (Fig. 3d) yet the proportion and salinity of HSSW in Terra Nova Bay and Joides Basin appears to be  
 284 overestimated (Fig. 3f). The bottom temperatures from NEMO indicate the presence of very warm waters, likely of





285 circumpolar origin right on the eastern continental shelf (Fig. 3e) whereas in observations this shelf is found to be cold and  
 286 the warm water confined offshore of the shelf break with only occasional intrusions (Bergamasco et al., 2003; Fig. 3b).  
 287 Again, there is no ISW in this standard configuration as there is no explicit model representation of ice shelf-ocean  
 288 interactions. Offshore bottom properties are slightly cooler than WOA in the model, but the AABW signature (AABW box  
 289 Fig. 3d) falls within the range reported from observations (Bergamasco et al., 2002; Bouillon et al., 2011; Silvano et al.,  
 290 2020).



291  
 292  
 293 Figure 3: Same as Fig. 2 but for the Ross Sea.

#### 294 295 296 **4 Impact of explicit sub-ice shelf circulation**

297  
 298 The following sections present results pertaining to the “Open” cavity run where the eORCA1 grid is extended under FRIS,  
 299 LCIS and RIS to allow for circulation within the cavities and explicit interaction with the base of these ice shelves.

##### 300 301 **4.1 Melt rates**

302  
 303 The average melt rate pattern for FRIS, LCIS and RIS is shown in Fig. 4 for the model simulation equivalent years 1995 to  
 304 2009, where orange indicates melt and purple shows refreezing. The average net melt rate for this time period is shown in



305 Table 1 and compared to Depoorter et al. (2013) from which the volumes for the prescribed melt rates were taken for the  
 306 reference configuration (“Closed”). Opening the cavities results in at least double the melt reported from Depoorter et al.  
 307 (2013). This discrepancy reflects both a warm bias on the continental shelf in NEMO (Sect. 4.4) and a possible bias in  
 308 Depoorter's estimates which are lower than all other satellite estimates (Table 1). The net melt rates of each ice shelf from  
 309 various other observational and model studies are also listed in the table showing the wide spread in basal melt estimates  
 310 both within values calculated from observations and between observations and models (Table 1). The model studies of  
 311 Mathiot et al. (2017) and Bull et al. (2021), which are both regional NEMO 1/4° configurations, and the NEMO 1/12°  
 312 configuration of the southwestern Weddell Sea of Haussmann et al. (2020), are particularly relevant to compare eORCA1  
 313 with, as here we see the possible impact of lowering the resolution in NEMO. For the Weddell Sea, our global 1° (eORCA1)  
 314 compares well with these regional high resolution studies producing a net basal melt within 12 Gt/yr of the other estimates  
 315 for FRIS and LCIS. The eORCA1 melt rate for RIS, while being higher than observational studies, is in the middle of other  
 316 model estimates, and is especially well aligned with that of NEMO 1/4° from Mathiot et al. (2017). Overall, eORCA1's net  
 317 melt rates correspond well with the average from all other estimates and are well within the standard deviations (last line of  
 318 Table 1).  
 319

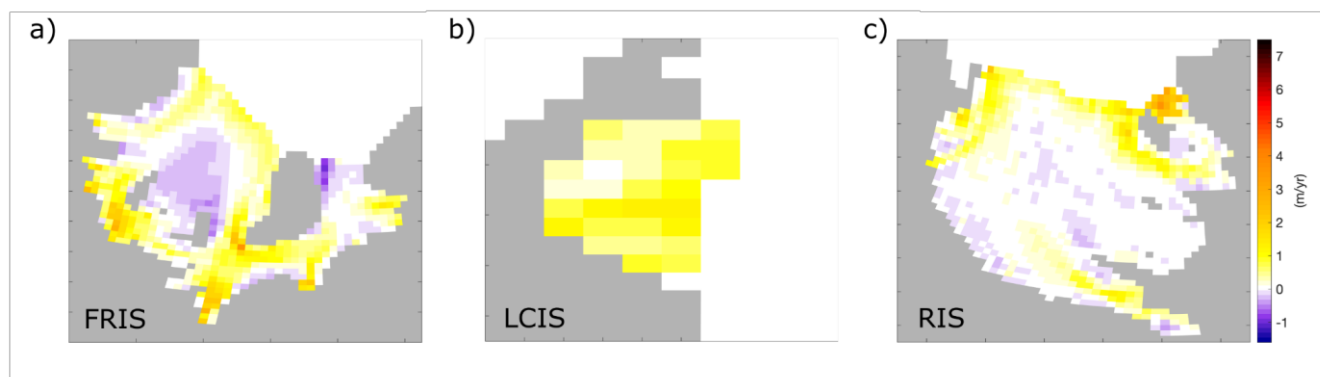
	<i>Values in Gt/yr</i>	<b>FRIS</b>	<b>LCIS</b>	<b>RIS</b>
	<b>NEMO 4.2 eORCA1 (1995-2009)</b>	117 ± 21	36 ± 7	112 ± 22
<b>Obs</b>	<b>Depoorter et al., 2013 (1995-2009)</b>	50 ± 40	18 ± 8	34 ± 25
	<b>Adusumilli et al., 2020 (1994-2018)</b>	81 ± 123	78 ± 99	80 ± 82
	<b>Rignot et al., 2013 (2003-2008)</b>	155 ± 36	21 ± 67	48 ± 24
	<b>Moholdt et al., 2014 (2003-2009)</b>	124		50
<b>Models</b>	<b>Mathiot et al., 2017 (1988)</b>	123	46	111
	<b>Timmermann et al., 2012(1980-1999)</b>	138	48	260
	<b>Hellmer et al., 2004 (1978-1997)</b>	119	38	180
	<b>Naughten et al., 2018 (FESOM HR) (2002-2016)</b>	115	55	112
	<b>Naughten et al., 2018 (MetROMS) (2002-2016)</b>	46	18	54
	<b>Haussmann et al., 2020 (1993-1997)</b>	105	24	
	<b>Bull et al., 2021 (1986-2017)</b>	124		
	<b>Average from all the above excluding present study</b>	111 ± 33	37 ± 21	118 ± 87

320  
 321 Table 1: Comparison of mean net melt rates (Gigatons per year) for Filchner-Ronne (FRIS), Larsen C (LCIS) and Ross Ice  
 322 Shelves (RIS) for observational and model studies. The mean and standard deviation of all the estimates depicted in the table  
 323 excluding the current study are shown at the bottom.  
 324

325 The patterns of melt shown in Fig. 4 also compare well with those of observational estimates like Rignot et al. (2013) and  
 326 high resolution model results like Haussmann et al. (2020) whose color bar we replicated for ease of cross-comparison. If we  
 327 look at the melt pattern of FRIS and compare it with these two aforementioned studies, we see that eORCA1 captures the



328 high melt rates at the western portion of the ice shelf front, at the southern edge of Berkner Island and along the grounding  
329 line at the back of the cavity. The model also correctly simulates the region of refreezing along the western boundary of the  
330 circulation cell within the cavity, in both the Ronne and Filchner depressions and the re-freezing in the shallow region  
331 between the Korff and Henry Ice Rises (Fig. 4a, see bathymetry location in Fig. 1b). For LCIS, the entire shelf shows a  
332 positive melt (Fig. 4b). Observations from Rignot et al. (2013) and simulations from Harrison et al. (2022) indicate some re-  
333 freezing under this ice shelf but the regional high resolution model studies of Mathiot et al. (2017) and Hausmann et al.  
334 (2020) similarly show melting only. The pattern for RIS generally compares well with that reported from observations but  
335 the magnitude of melt at the ice shelf front, especially to the east, is elevated (Fig. 4c).  
336



337  
338 Figure 4: Melt rates in meters per year for (a) Filchner-Ronne Ice Shelf, (b) Larsen C Ice Shelf and (c) Ross Ice Shelf where  
339 orange indicates melt and purple re-freezing. The results are mean values for the model equivalent period 1995-2009.  
340

341

## 342 4.2 Circulation and properties

343

344 Opening the sub-ice shelf cavities in eORCA1, allows for the establishment of a horizontal gyre circulation within the cavity  
345 and on the continental shelf of the Weddell and Ross Seas, in line with previous studies (Losch et al., 2008; Mathiot et al.,  
346 2017).

347

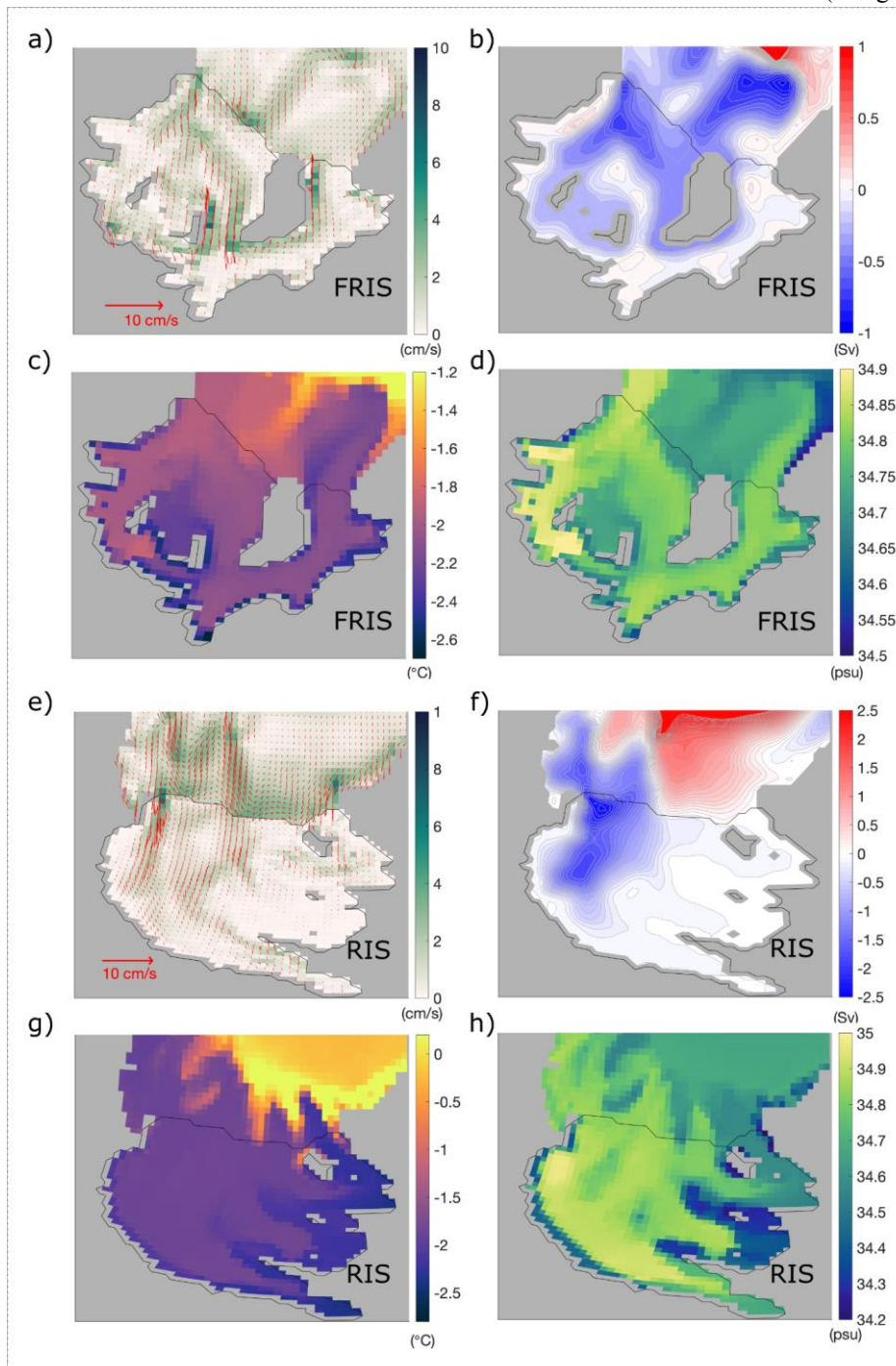
### 348 4.2.1 FRIS

349

350 The mean state of circulation from the last 10 years of simulation within the FRIS cavity, along with the associated bottom  
351 thermohaline properties can be seen in Figs. 5a-5d. The circulation patterns shown here are in good agreement with Bull et  
352 al. (2021) at  $1/4^\circ$  and with Hausmann et al. (2019) at  $1/12^\circ$  with the exception of higher bottom salinities in eORCA1 and a  
353 slightly weaker barotropic circulation strength. Note that here we use potential temperature and practical salinity so as to be  
354 in line with the other figures of this paper, so approximately 0.17 psu must be added when juxtaposing with absolute salinity  
355 plots. The depth averaged velocity and barotropic circulation pattern in Figs. 5a and 5b both indicate an anticlockwise  
356 circulation under the ice shelf. Comparatively warm and salty HSSW enters via the Ronne Depression, circulates from west  
357 to east, melting the base of the ice shelf mostly along the grounding line (cold, fresh signatures in Figs. 5c and 5d), and exits  
358 via the Filchner Trough as ISW. This pattern is consistent with observations (Nicholls et al., 2001; Janout et al., 2021). Two  
359 pathways of Modified Warm Deep Water (MWDW) towards the ice shelf front can be seen, both in the circulation pattern  
360 (Fig. 5a) and via the bottom temperature (Fig. 5c): one located in the middle of the continental shelf (Central Trough) and  
361 the other on the shelf to the east of Filchner Trough. These pathways provide a conduit for heat towards the ice shelf and



362 facilitate the mixing of shelf water masses with MWDW. It is therefore encouraging that eORCA1 captures these as they  
363 could play an important role in the evolution of FRIS shelf circulation in future climate scenarios (Naughten et al., 2021).



364  
365 Figure 5: Circulation pattern and characteristics of properties under Filchner Ronne (a-d) and Ross (e-h) ice shelves for the  
366 last 10 years of the open cavity experiment. Subplots (a) and (e) show depth averaged velocity, (b) and (f) barotropic stream



367 function, (c) and (g) bottom potential temperature and (d) and (h) bottom practical salinity (as opposed to conservative and  
368 absolute shown in Bull et al., 2021).

369

#### 370 **4.2.2 RIS**

371

372 Moving now to the Ross Sea, the time mean circulation pattern under RIS along with the bottom temperature and salinity  
373 can be seen in Figs. 5e-5h. Here we notice a strong anticlockwise circulation concentrated at the western boundary with  
374 reduced magnitude currents towards the back and east of the cavity. The west of the cavity is overall warmer and saltier and  
375 the east shows signatures of ISW. Bottom temperature indicates the presence of a cold ISW plume exiting the cavity to the  
376 far east (Fig. 5g) which is not seen in the time averaged velocities or barotropic streamfunction, likely because the associated  
377 speeds are extremely slow. Instead, the simulated circulation indicates an offshore advection of sub-ice shelf water following  
378 the Challenger Trough (see location marked in Fig. 1a). This water mass is likely recirculated HSSW as its temperature  
379 remains at surface freezing point (-1.9 °C). A strong clockwise circulation cell offshore of RIS (red in Fig. 5f) brings warm  
380 CDW into contact with the ice shelf front to the east, mixing out the signature of ISW further offshore (Fig. 5g). While this  
381 simulated circulation pattern agrees well with that described by observations (Fig. 1; Bergamasco et al., 2003; Budillon et  
382 al., 2003), it is likely too strong, resulting in an exaggerated net melt rate compared to the observational estimates (Table 1;  
383 anomalously high melt at the eastern portion of the ice shelf front in Fig. 4c).

384

385

#### 386 **4.3 Impact on offshore properties**

387

388 To highlight the impact of opening the FRIS, LCIS and RIS sub-ice shelf cavities on the offshore properties, Figs. 2g and 3g  
389 show the temperature versus salinity distribution excluding the data under the ice shelves. The differences in bottom  
390 temperature and salinity can be seen in Figs. 2h and 2i for the Weddell Sea and 3h and 3i for the Ross Sea.

391

392 A significant improvement in the representation of Weddell shelf water properties is evident as now HSSW is within the  
393 observed range and ISW is detected on the continental shelf (see HSSW and ISW red boxes in Fig. 2g). Opening the sub-ice-  
394 shelf cavity of FRIS has allowed the HSSW that previously built up in the Ronne Depression to advect under the ice shelf,  
395 become modified through basal interactions and exit the cavity as colder and fresher ISW. Consequently, the temperature  
396 and salinity differences are polarized west and east with warmer fresher conditions along the entire western boundary of the  
397 Weddell Gyre and cooler saltier conditions on the eastern continental shelf (Figs. 2h and 2i). These results agree well with  
398 those of Mathiot et al. (2017). The impact of opening LCIS can be seen via the maintenance of cold bottom properties  
399 immediately to the north (despite the fact that the shelf circulation has changed so that HSSW no-longer floods this region),  
400 along with the presence of a large negative salinity anomaly indicative of ice shelf melt (Fig. 2i). As the simulation is only  
401 124 years long, the impact of opening the cavities on AABW cannot be fully assessed due to the slow renewal of this water  
402 mass at the bottom of the global ocean. A small change in signature of AABW can, however, be seen in the volumetric T-S  
403 plot (supplementary material Fig. S1a) where explicit ocean-ice shelf interaction results in a shift in volume towards fresher,  
404 slightly cooler AABW. This shift is accompanied by a small increase in volume of the water mass by 0.23 % (AABW limits  
405 delineated in green in Fig. S1a).

406

407 The impact of opening the RIS cavity on offshore properties can be seen in Figs. 3h and 3i. Similar to the Weddell Sea,  
408 conditions in the west where in the reference run HSSW was built up, now become warmer and fresher as the path under the  
409 ice shelf is open. The signature of the cold plumes of dense shelf water (Fig. 5g) on either side of Roosevelt Island can  
410 clearly be seen in the temperature difference plot (Fig. 3h), but curiously they do not possess the same salinity anomaly (Fig.

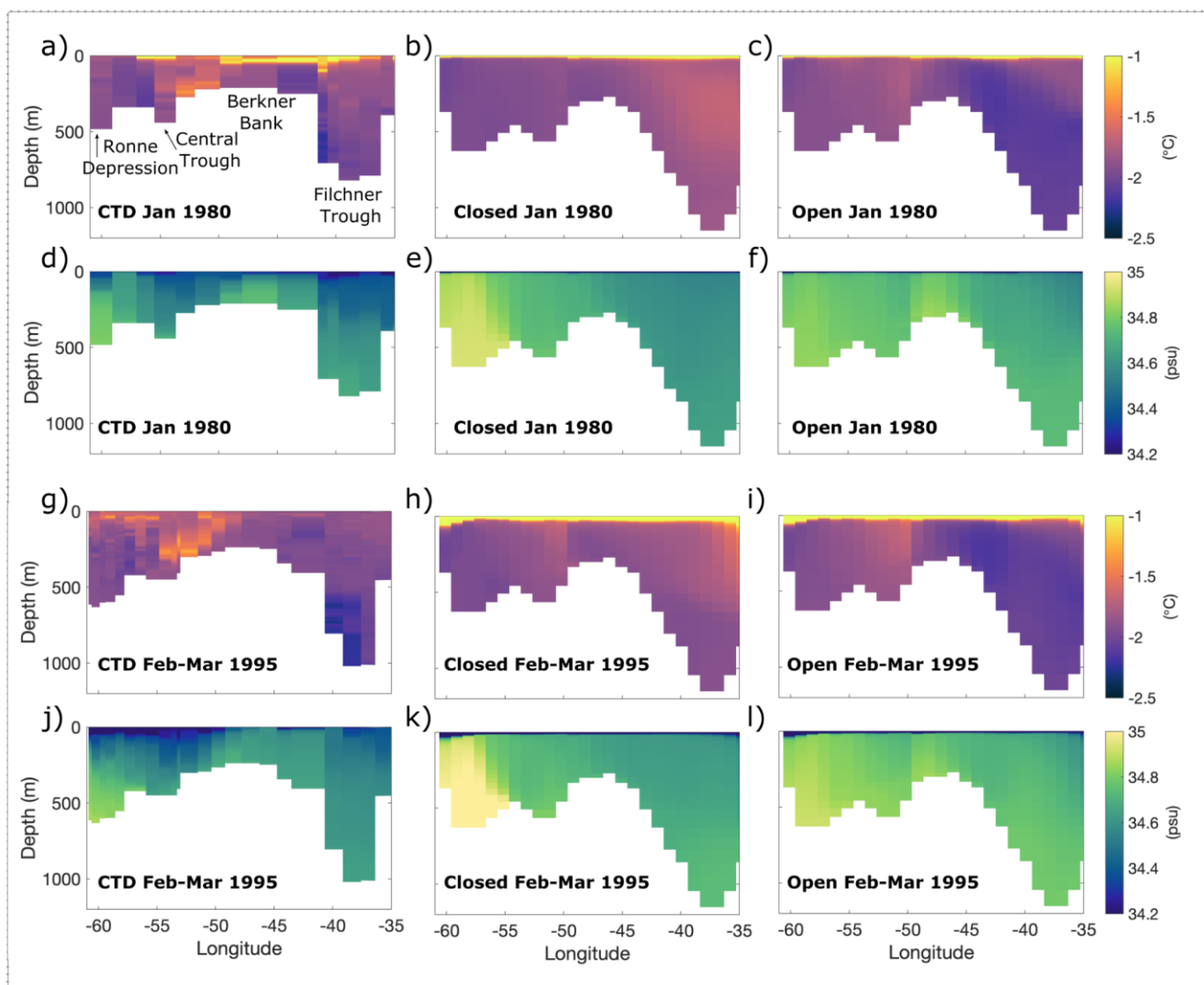


3i). The positive salinity difference of the western plume indicates that this water is a variety of HSSW which has circulated under the ice shelf and was previously not present in this area. The small negative anomaly to the east indicates that this cold plume is, as previously hypothesized, outflowing ISW. Small temperature differences on the continental slope and further offshore indicate that there has been some communication of the changes in shelf waters further afield. The volumetric T-S plot for the Ross Sea found in supplementary material (Fig. S1b) indicates that opening the RIS cavity has moved the core of AABW towards cooler fresher values, accompanied by a 0.34 % decrease in volume of AABW as defined by the original water mass limits (delineated in green in Fig. S1b).

#### 4.4 Comparison with ice shelf front CTD observations

The differences in circulation patterns and in thermohaline properties that result from opening the RIS and FRIS cavities documented above do not elucidate whether or not we have reduced biases and improved the realism shelf waters in eORCA1. For this, a direct comparison with in-situ observations is necessary. Due to the remote location of these ice shelves and the harsh conditions associated with obtaining hydrographic samples in these areas, there are limited observations, and so optimally interpolated atlases such as WOA or ocean reanalysis products like SOSE miss important local features or seasonal variability. For comparison purposes, we have consequently selected CTD data from research cruises that have sampled transects across the front of the ice shelves and extracted the model data corresponding to the approximate ship's track using PAGO, a pre-existing tool to analyze gridded ocean datasets (Deshayes et al., 2014).

For FRIS we use two CTD sections across the ice shelf front undertaken in 1980 and 1995 on board the RV Polarstern by the Alfred Wegener Institute (Rohardt et al., 2016; Janout et al., 2021). The location of the section selected in NEMO to approximately overlay the CTD transects can be seen as a magenta dotted line in Fig. 1b. The output from NEMO corresponding to the same months and same equivalent year (for the second cycle of CORE forcing) in the simulation was selected for both "Closed" (prescribed freshwater flux) and "Open" (FRIS, LCIS and RIS) cavity runs. A comparison between the CTD data and NEMO can be seen in Figs. 6a to 6f for January 1980 and Fig. 6g to 6l for February to March 1995. In terms of surface waters, NEMO does not capture the fine scale horizontal variability and overestimates the subsurface salinity. For both observational years, evidence of warm, fresh, MCDW intrusions can be seen in the middle of the CTD sections (Central Trough; Figs. 6a and 6g). While the model struggles to capture the coherence of this sub-surface temperature maximum, the counterclockwise circulation cell setup on the central continental shelf in the open cavity simulation does aid the advection of MCDW towards the ice shelf, thereby producing a slightly better representation of this warm intrusion in Figs. 6c and 6i. The presence of cold ISW in Filchner Trough is clearer in the 1995 CTD data than in 1980 where the sampling frequency was sparser and this region not well covered. The 2018 Polarstern sampling of the Jason Trough was the highest resolution yet and while we cannot directly compare with the simulation output as the CORE forcing ends in 2009, evidence for the presence of a tongue of ISW focused on the western bank of Filchner Trough is evident in Fig. 3 of Janout et al. (2021) and so should be kept in mind for comparison. Opening the FRIS cavity overall improves the thermohaline properties at the ice shelf front, most notably by spreading out the pool of HSSW from the Berkner Depression (e.g. Fig. 6k) across the continental shelf (e.g. Fig. 6l) and by facilitating the production and thus outflow of ISW within Filchner Trough (Figs. 6c and 6i).



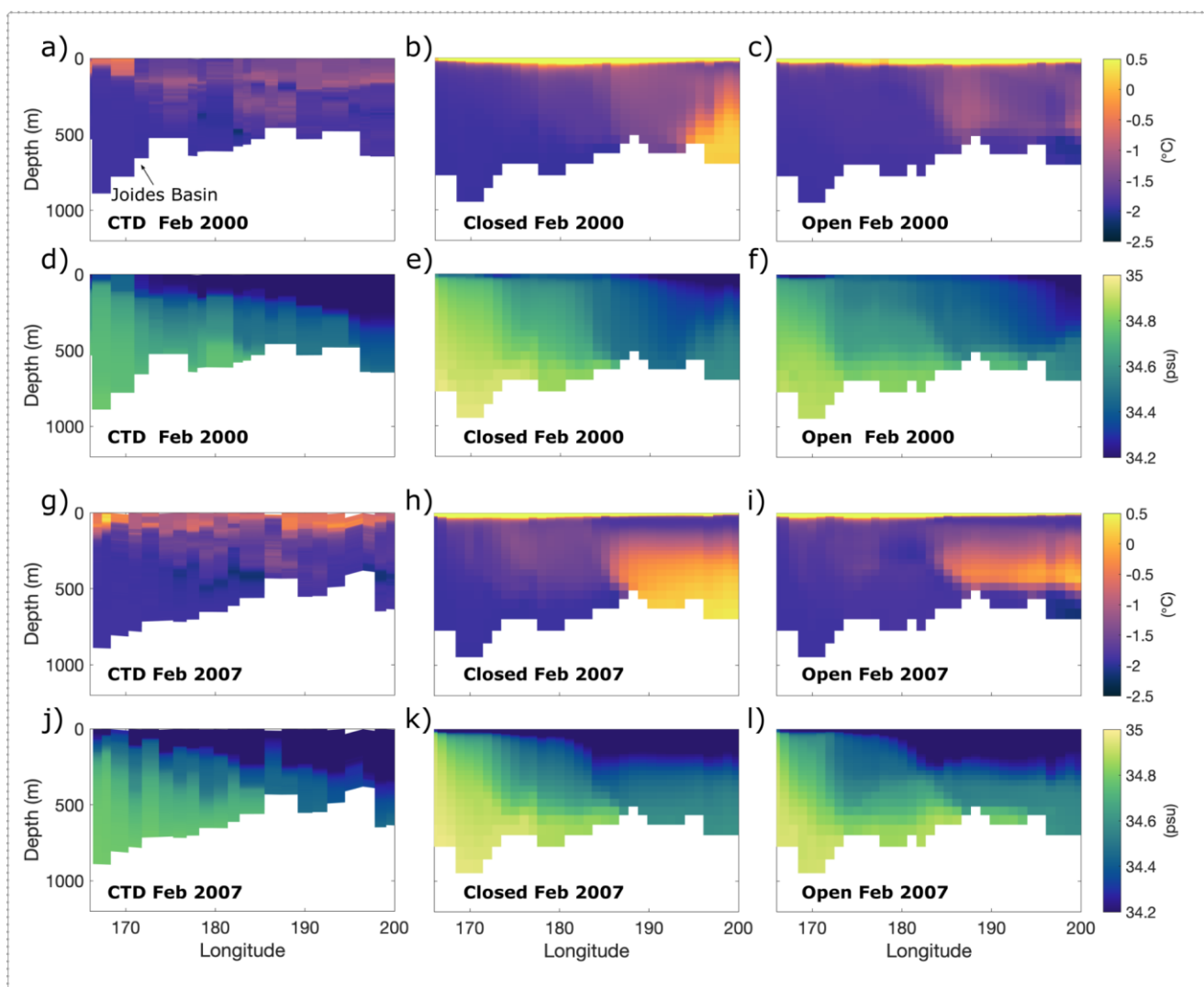
451  
452  
453  
454  
455  
456  
457  
458  
459  
460  
461  
462  
463  
464

Figure 6: Validation of properties across the Filchner Ronne Ice Shelf front by comparing closed and open cavity NEMO results with measured values from CTD sections performed in 1980 (Rohardt et al., 2016) and 1995 (Janout et al., 2021). The model output for the corresponding equivalent year and month was extracted for more accurate comparison. Bathymetric features discussed in the text are labelled in subplot (a).

The CTD sections used for comparison along the front of RIS were obtained through the World Ocean Circulation Experiment Database (Boyer et al., 2018) and correspond to cruises undertaken on board the RVIB Nathaniel B. Palmer in 2000 (cruise id: US010404; Smethie and Jacobs, 2005) and in 2007 (cruise id: US034357). Data was extracted from the eORCA1 simulation corresponding to the dates of these cruises and the approximate ship track across the ice shelf front (magenta dotted line in Fig. 1a). Similar to the Weddell Sea, the model tends to overestimate the subsurface temperature and salinity (Figs. 7b, 7e, 7h and 7k), suggestive of biases in the representation of coastal processes, including vertical mixing. This effect is somewhat reduced by allowing for circulation under RIS, especially by decreasing subsurface salinities (Figures



465 7f and 7l). At depth, NEMO captures the east-west distribution of haline properties such as the HSSW pool located within  
466 Joides Basin, albeit with somewhat amplified salinities. In terms of temperature, the model has a clear bias to the east,  
467 especially in the closed cavity run, where CDW is detected at the ice shelf front. Both the temperature and salinity biases are  
468 reduced in the open cavity run (e.g. Figs. 7c and 7f). In particular, the significant reduction in the extent and magnitude of  
469 the sub-surface warm water intrusions brings the model more in-line with observations.  
470



471  
472  
473 Figure 7: Same as Fig. 7 but for Ross Ice Shelf front for CTD sections performed in 2000 (Smethie and Jacobs, 2005) and  
474 2007 (Boyer et al., 2018).  
475  
476 A recurring theme throughout the results presented here is that the model is overall too salty, driven by what appears to be an  
477 over-production of HSSW in the Ronne Depression and Joides Basin. One driver for this could be the hyper-activity of dense  
478 water formation via open-ocean convection which forms the totality of parent waters of AABW in the absence of ice shelves





479 in eORCA1. This can be seen in Supplementary Material Fig. S2 where the mean winter (July-August-September) mixed  
480 layer depths (MLD) in the reference run for the years 1971-2009 (Fig. S2c and S2d) are compared to the climatology from  
481 Sallee et al. (2021) for the same time period and using the same criteria for calculation (Fig. S2a and S2b; MLD defined as  
482 the depth at which density exceeds the 10 m density by  $0.03 \text{ kg m}^{-3}$ ). The model greatly overestimates winter MLDs in the  
483 Weddell Sea, both on the continental shelf adjacent to FRIS where the depth of the base of the mixed layer aligns with  
484 bathymetric features indicating deep convection right to the ocean floor, and offshore of the continental slope where a large  
485 region of MLD greater than 1000m is present (Fig. S2c). This level of open ocean deep convection has in reality only once  
486 been observed, during the 1974-1976 Weddell Polynya, indicating a gross overestimation of winter MLDs in the model  
487 (Heuze et al., 2021; Killworth et al., 1983). Ross Sea MLDs (Fig. S2d) compare better with observations, but show values  
488 indicating a full water-column-depth convection in Terra Nova Bay which is not reported in Sallee et al. (2021). Curiously,  
489 NEMO actually under-estimates winter mixed layers in the eastern portion of the Ross continental shelf showing mean  
490 MLDs of under 100m where the observational climatology indicates values of around 400m (Fig. S2d compared to Fig.  
491 S2b). This too-strong stratification could be one of the factors facilitating the intrusion of CDW to the ice shelf front seen in  
492 Figs. 7b and 7h.

493  
494 Note that if ISW is explicitly formed, as in the open cavity experiment, the exaggerated deep convection on the shelf should  
495 be reduced, otherwise the signatures of ISW and modified HSSW will simply be mixed out. Some reduction in MLD is seen  
496 on the continental shelf and slope in the Filchner (Fig. S2e) and Challenger Troughs (Fig. S2f) due to the increase in  
497 stratification as a result of the greater bottom densities present in these areas (Fig. S5a and S5c) and surface freshening (Figs.  
498 8d and 9d). Conversely, the regions of exaggerated MLDs, offshore in the center of the gyre of the Weddell Sea, and in Terra  
499 Nova Bay in the Ross Sea actually deepen (positive anomalies Figs. S2e and S2f). This highlights the need for work to be  
500 done on reducing wintertime deep convection and would complement efforts underway on better representing dense water  
501 overflows.

502  
503 The authors note that the biased MLDs could be one of a number of factors driving the overly saline conditions; wrong sea-  
504 ice parameters and biases in the atmospheric forcing could also play an important role. High ice production is seen on the  
505 southwest continental shelves of the Weddell and Ross Seas in Supplementary Figs. S3c and S4c. Opening the cavities  
506 reduces the magnitude of ice production in the Ronne Depression (Fig. S3d) and at the location of the Terra Nova Bay  
507 Polynya (Fig. S4d) but increases the production of ice (and thus HSSW) further east. The result is a re-organisation of the  
508 locations of HSSW formation and a redistribution of the continental shelf circulation. This does not fully correct for the net  
509 over production of HSSW and thus the positive salt bias seen in Figs. 6 and 7, but it does work towards decreasing bottom  
510 salinities offshore (Figs. 2i and 3i) and bringing the HSSW signature more in line with observations (Figs. 2g and 3g). Please  
511 see the Supplementary Information for an in-depth evaluation of simulated sea ice near the studied ice shelves and a  
512 diagnosis on the effect of opening the cavities on sea ice.

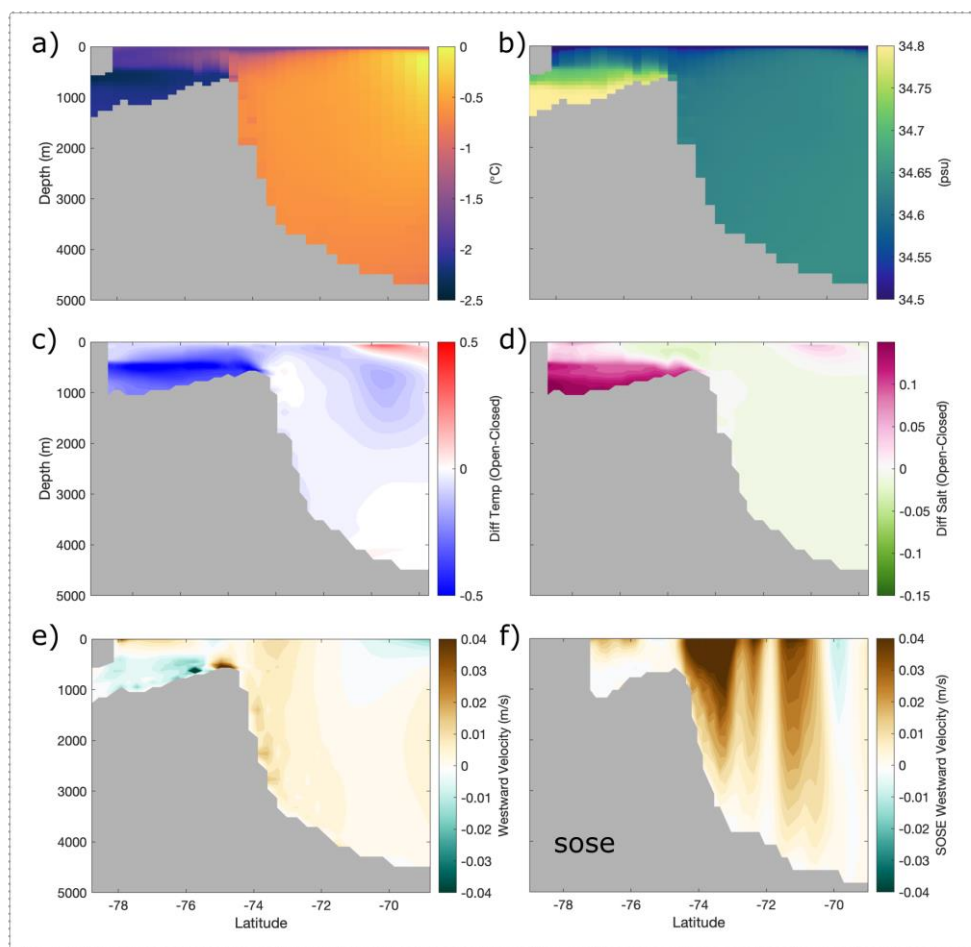
#### 513 514 **4.5 Offshore export of continental shelf properties**

515  
516 We have seen how opening the large, cold, ice shelf cavities in eORCA1 leads to a better representation of continental shelf  
517 circulation and thermohaline property distributions. But the question remains regarding the transfer of these now more  
518 realistic dense shelf waters, offshore, to feed the globally important AABW. While the simulation period of 124 years (2  
519 CORE forcing cycles) is too-short to explore the impact of these changes far-afield, it is sufficient to investigate the changes  
520 on the continental shelf and slope adjacent to the large ice shelves. To do this, we use PAGO (Deshayes et al., 2014) to select  
521 a cross section of data following the bathymetric troughs of the Weddell and Ross Seas which are thought to be important for  
522 dense water export, namely the Filchner and Challenger Troughs (sections shown in green in Fig. 1).



523  
524  
525  
526  
527  
528  
529  
530

The thermohaline and velocity cross sections of Filchner Trough and a continuation down the continental slope can be seen in Figs. 8a and 8b for the open cavity run and the difference between these values and the reference run (Open-Closed) are shown in Figs. 8c and 8d. By opening the sub-ice shelf cavity, the properties within Filchner Trough have decreased in temperature and increased in salinity as the candidate-parent waters of AABW build up on the continental shelf. This results in a net increase in density at the bottom of the trough (Fig. S5b), but there is very little indication of a coherent cascading of this water down the continental slope.



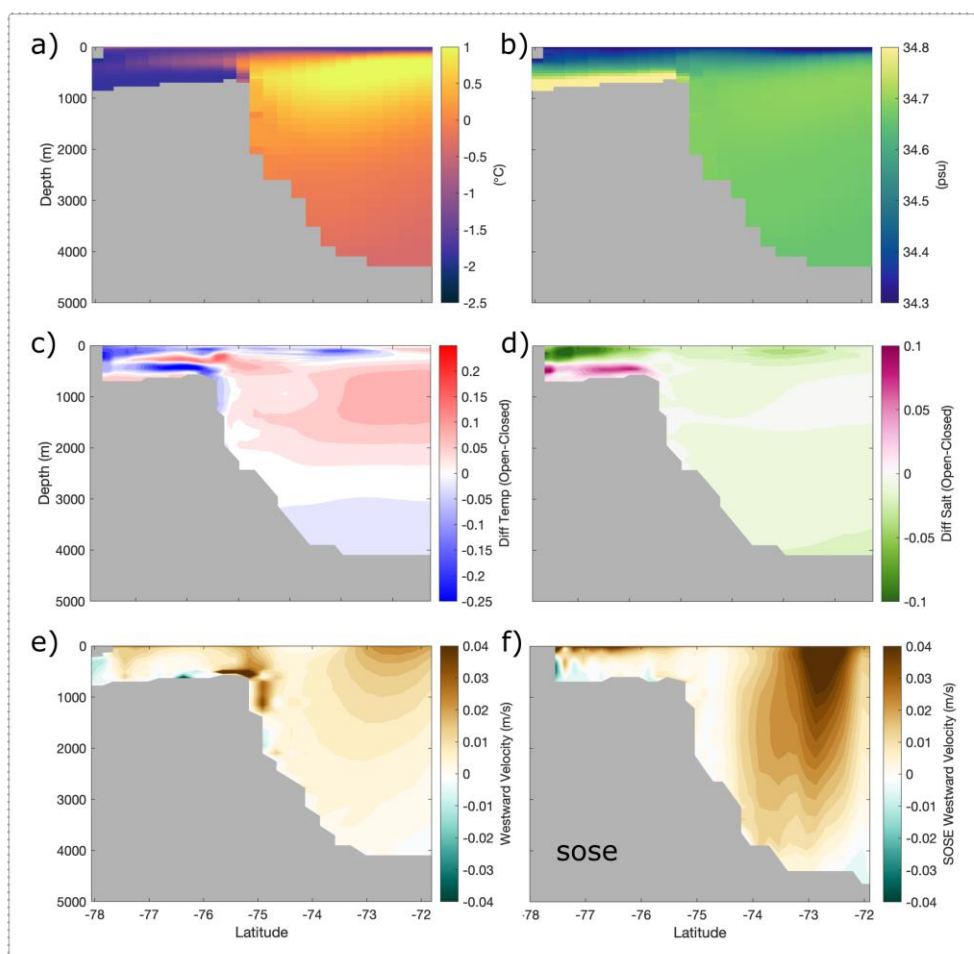
531  
532  
533  
534  
535  
536  
537  
538  
539

Figure 8: Cross section of properties along the Filchner Trough and down the adjacent continental slope of the Weddell Sea for (a)-(e) NEMO and (f) SOSE. Subplots (a) and (b) show temperature and salinity for the open cavity configuration, to be compared to (c) and (d) which show the differences (Open - Closed) with the reference configuration. Subplot (e) shows cross sectional velocities with westward as positive for the open cavity run, to be compared with SOSE values shown in subplot (f).

A cross section of the Challenger Trough (Fig. 9), reveals depth-varying thermohaline changes as opening the sub-ice shelf cavity has allowed for the water adjacent to the ice shelf to advect into the cavity leaving the bottom properties here slightly



540 warmer, while the layer immediately above experiences cooling and salinification due to the outflow of ISW driven by the  
541 'ice pump' (Fig. 9c). Here we see some evidence indicating the translation of this dense cold water tongue over the  
542 continental shelf break and downslope (Figs. 9c and S5d). The overflow of this water results in the pulling in of warmer  
543 offshore water at intermediate depth (Fig. 9c). A horizontal redistribution of surface waters simultaneously takes place due  
544 to the anti-clockwise circulation pattern (Fig. 5e) which in turn produces a cooling and freshening in the surface layer (Figs.  
545 9c and 9d).  
546



547  
548 Figure 9: Same as Fig. 9 but for the Challenger Trough and the Ross Sea continental slope.  
549

550 For both the Filchner and Challenger Troughs, the downslope export of the ISW tongue is limited due to the commonly-  
551 known and acknowledged problem of correctly capturing this overflow in a coarse z-coordinate model (Heuze et al., 2021).  
552 The aptitude of representing dense water overflows is thought to increase with models of higher resolution, but this is  
553 difficult to achieve in a global model for climate coupling purposes without a nested zoom (Storkey et al., 2018; Solodoch et  
554 al., 2022).  
555



556 Another important dynamic for Antarctic shelf water realism is the Antarctic Slope Current (ASC; red arrows in Fig. 1) and  
557 related Antarctic Slope Front, which together restrict the lateral mixing of offshore and shelf water masses, acting as an  
558 effective barrier protecting the large cold ice shelves from warm water masses of circumpolar origin (Thompson et al.,  
559 2018). Some CDW, or a modified version thereof, is carried within the ASC and occasionally fluxes onshore to mix with  
560 dense shelf waters (Beadling et al., 2020; Bull et al., 2021). This interaction between dense shelf water and CDW is  
561 important for the formation of AABW, as the onshore flux of water replaces the dense water transported offshore and thus  
562 sustains formation of shelf water (Thompson et al., 2018). Figure 8e shows a velocity cross section for the Weddell Sea shelf  
563 and slope where westward velocities are positive so as to correspond with the direction of the ASC and the net westward  
564 transport across the section is 9.8Sv. This can be compared to Fig. 8f which is a cross section from SOSE output (same time  
565 periods used) where the net transport is three times higher at 32.8Sv. Similarly for the Ross Sea, Fig. 9e shows a cross  
566 section of westward velocities in eORCA1 where the volume transport is 13.3Sv which is less than half of that estimated  
567 from SOSE in Fig. 9f of 20.9Sv. As can be seen from both SOSE cross sections, the ASC flows eastward as a narrow jet,  
568 closely following the shelf break in the Weddell Sea and slightly further offshore in the Ross Sea. It is well known that  
569 coarse resolution models are unable to correctly represent the ASC as a resolution of at least  $0.5^\circ$  is needed to capture the  
570 dynamics and net transport (Mathiot et al., 2011). The absence of realistic ASC in NEMO eORCA1 (Figs. 8e and 9e) has  
571 important consequences for the onshore-offshore exchange of water masses and is a restriction that needs to be kept in mind  
572 when using this coarse resolution configuration for process studies in the area.

573  
574

## 575 **5 Discussion**

576

577 Explicitly representing ocean-ice shelf interactions is of great interest to modelers as these processes play an important role  
578 in global ocean dynamics, climate and future sea level rise. The formation of dense shelf waters (HSSW and ISW) along the  
579 Antarctic coastline provides the principal source for AABW, which in turn facilitates the ventilation of the deep ocean and  
580 constitutes the lower limb of the global overturning circulation (Killworth, 1983; Johnson, 2008; Orsi, 2010).

581

582 Our results focus on the Weddell and Ross seas as they are respectively the main ventilation source of the abyssal Atlantic  
583 and Indian basins, and the abyssal Pacific basin (Solodoch et al., 2022). Explicitly simulating the sub-ice shelf cavities of  
584 FRIS and LCIS in the Weddell Sea leads to a re-organisation of continental shelf circulation with thermohaline patterns in  
585 agreement with those reported by other NEMO model studies (Mathiot et al., 2017; Storkey et al., 2018 and Bull et al.,  
586 2021), namely warming and freshening in the west and cooling and salinification in the east. Notably, opening a pathway for  
587 HSSW under FRIS allows for an anticlockwise circulation of water under the ice shelf, triggering basal melt and re-freezing,  
588 and producing the super-cold ISW. In both the Weddell and Ross Seas, opening the cavities decreases sea ice production to  
589 the west of the ice shelves, assisting in the partial reduction of the salt bias in these areas linked to polynya activity.

590

591 By comparing model output with two CTD sections performed across the front of FRIS in 1980 and 1995 (Rohardt et al.,  
592 2016; Janout et al., 2021), we see clear evidence of an improvement in the realism of water properties with the opening of  
593 the sub-ice shelf cavity. Similarly in the Ross Sea, an anticlockwise sub-ice shelf cavity circulation cell facilitates the spread  
594 of HSSW across the continental shelf and ocean-ice shelf interactions create a cold ISW plume to the east of Roosevelt  
595 Island. By evaluating the model output against CTD sections performed in 2000 and 2007 (Smethie and Jacobs, 2005; Boyer  
596 et al., 2018), we see that opening the cavity significantly ameliorates the sub-surface warm water bias otherwise seen to the  
597 east of RIS in the reference configuration, and brings a significant improvement in the horizontal thermohaline distributions.

598



599 The net melt rates of FRIS, LCIS and RIS are found to be within the uncertainty range of observational estimates and other  
600 model studies. Notably, the melt rate pattern of FRIS agrees surprisingly well with the high resolution regional model of  
601 Haussmann et al. (2020) and the satellite observations of Rignot et al. (2013), showing details of melt and refreezing that  
602 were not expected at a 1° resolution, although the meanders of the grounding line are not well represented at 1°. For RIS, the  
603 net melt is higher than all observed estimates but lower than that predicted by other model studies. RIS melt rates are  
604 strongly related to the supply of warm water to the ice shelf base (Arzeno et al., 2014), and correctly representing this in  
605 models presents a challenge due to the close proximity of CDW to the ice shelf front in this area.

606  
607 Meltwater and modified HSSW mix on the continental shelves of the Weddell and Ross Sea and in reality cascade down the  
608 continental slope, mixing with ambient water masses during the descent, to eventually feed AABW. This process is poorly  
609 represented in NEMO eORCA1, a common problem with coarse z-coordinate models, as exaggerated vertical and horizontal  
610 mixing erodes the signatures of the dense overflow tongue. As mentioned by Storkey et al. (2018), the use of a terrain  
611 following coordinate system (known as sigma coordinate) can greatly improve the representation of these density currents,  
612 and so is something worth exploring in the future. Improvement in the representation of the overflows along with a reduction  
613 of open-ocean deep convection should together allow for a coherent communication of the now more realistic properties of  
614 dense water on the continental shelf offshore to AABW.

## 615 616 **6 Conclusion**

617  
618 In this paper the authors focus on improving the properties of AABW parent waters in a global NEMO configuration. We  
619 compare the model simulations with local in situ observations, in addition to gridded climatologies, so as to deepen  
620 understanding and expertise regarding the impact of opening sub-ice shelf cavities on ocean dynamics. As ocean models  
621 used for climate simulations with multiple scenarios (such as CMIP) need to be at a coarse resolution to permit long  
622 integrations, we use the NEMO global ocean 1° configuration, eORCA1, here. The results presented are for CORE inter-  
623 annual forcing, with a fixed cavity geometry, as this allows us to clearly identify the impact of ocean-ice shelf interactions at  
624 a few critical locations without the obscuring effect of coupling feedbacks. We present here a validated configuration of  
625 NEMO 4.2 eORCA1 with explicit ocean-ice shelf interactions only within the largest 3 cold-core cavities: FRIS, LCIS and  
626 RIS. Limitations of this choice are that together FRIS, LCIS and RIS only represent 63 % of the total area of Antarctic ice  
627 shelves and while they are responsible for the formation of the majority of the parent waters of AABW, interactions with  
628 remote unresolved ice shelves is missing (Nakayama et al., 2020). The next steps in terms of increasing complexity in  
629 NEMO eORCA1 are to open other intermediate size cavities, such as Amery, Riiser-Larsen and Fimbul, in a fixed geometry  
630 configuration. As the residence time needed to flush these smaller cavities is shorter than for FRIS and RIS, we suggest that  
631 the complex initialization methods presented here are not needed. This work is aimed at building understanding so as to  
632 eventually move to coupling with an ice sheet model thereby allowing for fully evolving cavity geometry and iceberg  
633 calving from the ice shelf front.

634  
635 Given the critical role that the Southern Ocean plays in regulating global climate, it is paramount that ocean models work  
636 towards improving the representation of key processes in order to provide state-of-the-art simulations of the ocean in a  
637 changing climate (Beadling et al., 2020). The global configuration of NEMO presented here, has been proven to improve the  
638 realism of water masses in the Weddell and Ross Seas. We advocate for climate modelers to use it, as it enables a more  
639 accurate representation of the formation of the parent waters of AABW, and a first step in the perspective of representing  
640 ocean-ice shelf interactions in climate applications.

641  
642



643

## 644 **7 Author contribution**

645

646 KH, JD and PM together contributed to the conceptualization of the research outlined in this manuscript. KH led the formal  
647 analysis and investigation with the assistance of JD, CR, CL, NJ and PM. MV led the sea ice research component with  
648 assistance from CL. Validation of the model was undertaken by KH with PM. CE led the programming, code management  
649 and supervised all the model runs undertaken by KH. The project was supervised by JD and NJ, providing guidance and  
650 critical feedback. The whole group contributed to the writing and review of the submitted manuscript.

651

## 652 **8 Competing interests**

653

654 The authors declare that they have no conflict of interest.

655

## 656 **9 Acknowledgements of financial support**

657

658 Katherine Hutchinson received financial support of the European Union's Horizon 2020 research and innovation programme  
659 Marie Skłodowska-Curie grant agreement No 898058 (Project OPEN). Nicolas Jourdain received support from the European  
660 Union's Horizon 2020 research and innovation programme under grant agreement no. 101003536 (ESM2025). Pierre  
661 Mathiot acknowledges support from the European Union's Horizon 2020 research and innovation programme under grant  
662 agreement no. 820575 (TiPACCs). This work was performed using HPC resources from GENCI–IDRIS (Grant 2021-  
663 A0100107451) and from the IPSL Mesocentre ESPRI.

664

## 665 **10 Code and data availability**

666

667 The NEMO ocean model code is available via open software license from the NEMO website (<https://www.nemo-ocean.eu>).  
668 The NEMO output for the Weddell and Ross Seas (focus of this study), plus the namelists used, bathymetry, ice shelf draft,  
669 freshwater input and initial condition files are available via the data repository stored here:

670 <https://doi.org/10.5281/zenodo.7561767>. Some example scripts for data extraction, calculations and plotting can also be  
671 found in this repository. The World Ocean Atlas hydrographic data of Locarnini et al. (2019) and Zweng et al. (2018) can be  
672 found here: <https://www.nodc.noaa.gov/OC5/woa18/woa18data.html> and Southern Ocean State Estimate data of Mazloff et  
673 al. (2010) can be accessed here: [http://sose.ucsd.edu/sose\\_stateestimation\\_data\\_05to10.html](http://sose.ucsd.edu/sose_stateestimation_data_05to10.html). The mixed layer depth data  
674 from Sallee et al. (2021) can be accessed here: <https://doi.org/10.5281/zenodo.5776180>. The CTD transects used for  
675 comparisons across the ice shelf front for FRIS 1980 and 1995 can be respectively found here:

676 <https://doi.org/10.1594/PANGAEA.860066> and here <https://folk.uib.no/ngfso/Data/CTD/>. The RIS CTD data from the 2000  
677 (US010402) and 2007 (US034357) RVIB Nathaniel B. Palmer cruises are available from the World Ocean Data Base at  
678 [https://www.nodc.noaa.gov/OC5/WOD/pr\\_wod.html](https://www.nodc.noaa.gov/OC5/WOD/pr_wod.html). The PAGO toolbox used to extract model output along a line in front  
679 of the ice shelf from Deshayes et al. (2014) can be accessed here: <https://www.whoi.edu/science/PO/pago/>.

680

681

682

683



684 **References**

- 685 Abrahamsen, E. P., Meijers, A. J., Polzin, K. L., Naveira Garabato, A. C., King, B. A., Firing, Y. L., Sallée, J., Sheen, K. L.,  
686 Gordon, A. L. and Huber, B. A.: Stabilization of dense Antarctic water supply to the Atlantic Ocean overturning circulation,  
687 Nature Publishing Group, 2019.
- 688 Adusumilli, S., Fricker, H. A., Medley, B., Padman, L. and Siegfried, M. R.: Interannual variations in meltwater input to the  
689 Southern Ocean from Antarctic ice shelves, Nature Publishing Group, 2020.
- 690 Arndt, J. E., Schenke, H. W., Jakobsson, M., Nitsche, F. O., Buys, G., Goleby, B., Rebesco, M., Bohoyo, F., Hong, J. and  
691 Black, J.: The International Bathymetric Chart of the Southern Ocean (IBCSO) Version 1.0—A new bathymetric  
692 compilation covering circum-Antarctic waters, Wiley Online Library, 2013.
- 693 Asay-Davis, X. S., Cornford, S. L., Durand, G., Galton-Fenzi, B. K., Gladstone, R. M., Gudmundsson, G. H., Hattermann,  
694 T., Holland, D. M., Holland, D. and Holland, P. R.: Experimental design for three interrelated marine ice sheet and ocean  
695 model intercomparison projects: MISMIP v. 3 (MISMIP ), ISOMIP v. 2 (ISOMIP ) and MISOMIP v. 1 (MISOMIP1),  
696 Copernicus GmbH, 2016.
- 697 Beadling, R. L. L., Russell, J. L., Stouffer, R., Mazloff, M. R., Talley, L. D., Goodman, P. J., Sallee, J. B., Hewitt, H., Hyder,  
698 P. and Pandde, A.: Simulation of Southern Ocean Properties Across Model Generations and Future Changes under  
699 Continued 21 st Century Warming in CMIP6. 2020.
- 700 Bergamasco, A., Defendi, V., Zambianchi, E. and Spezie, G.: Evidence of dense water overflow on the Ross Sea shelf-break,  
701 Cambridge University Press, 2002.
- 702 Bergamasco, A., Defendi, V., Del Negro, P. and Umani, S. F.: Effects of the physical properties of water masses on  
703 microbial activity during an Ice Shelf Water overflow in the central Ross Sea, Cambridge University Press, 2003.
- 704 Bitz, C. M., Holland, M. M., Weaver, A. J. and Eby, M.: Simulating the ice-thickness distribution in a coupled climate  
705 model, Wiley Online Library, 2001.
- 706 Bowen, M. M., Fernandez, D., Forcen-Vazquez, A., Gordon, A. L., Huber, B., Castagno, P. and Falco, P.: The role of tides  
707 in bottom water export from the western Ross Sea, Nature Publishing Group, 2021.
- 708 Boyer, T.P., O.K. Baranova, C. Coleman, H.E. Garcia, A. Grodsky, R.A. Locarnini, A.V. Mishonov, C.R. Paver, J.R.  
709 Reagan, D. Seidov, I.V. Smolyar, K. Weathers, M.M. Zweng. : World Ocean Database 2018. A.V. Mishonov, Technical Ed.,  
710 NOAA Atlas NESDIS 87, 2018.
- 711 Budillon, G., Pacciaroni, M., Cozzi, S., Rivaro, P., Catalano, G., Ianni, C. and Cantoni, C.: An optimum multiparameter  
712 mixing analysis of the shelf waters in the Ross Sea, Cambridge University Press, 2003.
- 713 Bull, C. Y., Jenkins, A., Jourdain, N. C., Vaňková, I., Holland, P. R., Mathiot, P., Hausmann, U. and Sallée, J.: Remote  
714 Control of Filchner-Ronne Ice Shelf Melt Rates by the Antarctic Slope Current, Wiley Online Library, 2021.
- 715 Cao, J., Wang, B., Yang, Y., Ma, L., Li, J., Sun, B., Bao, Y., He, J., Zhou, X. and Wu, L.: The NUIST Earth System Model  
716 (NESM) version 3: description and preliminary evaluation, Copernicus GmbH, 2018.
- 717 Comeau, D., Asay-Davis, X. S., Begeman, C. B., Hoffman, M. J., Lin, W., Petersen, M. R., Price, S. F., Roberts, A. F., Van  
718 Roekel, L. P. and Veneziani, M.: The DOE E3SM v1. 2 Cryosphere Configuration: Description and Simulated Antarctic Ice-  
719 Shelf Basal Melting, Wiley Online Library, 2022.
- 720 Depoorter, M. A., Bamber, J. L., Griggs, J. A., Lenaerts, J. T., Ligtenberg, S. R., van den Broeke, M. R. and Moholdt, G.:  
721 Calving fluxes and basal melt rates of Antarctic ice shelves, Nature Publishing Group, 2013.



- 722 Deshayes, J., Curry, R. and Msadek, R.: CMIP5 model intercomparison of freshwater budget and circulation in the North  
723 Atlantic, 2014.
- 724 Dufresne, J., Foujols, M., Denvil, S., Caubel, A., Marti, O., Aumont, O., Balkanski, Y., Bekki, S., Bellenger, H. and  
725 Benshila, R.: Climate change projections using the IPSL-CM5 Earth System Model: from CMIP3 to CMIP5, Springer, 2013.
- 726 Fahrbach, E., Rohardt, G., Scheele, N., Schröder, M., Strass, V. and Wisotzki, A.: Formation and discharge of deep and  
727 bottom water in the northwestern Weddell Sea, Sears Foundation for Marine Research, 1995.
- 728 Goosse, H., Dalaiden, Q., Cavitte, M. G. and Zhang, L.: Can we reconstruct the formation of large open-ocean polynyas in  
729 the Southern Ocean using ice core records? Copernicus GmbH, 2021.
- 730 Gordon, A. L. : Interocean exchange of thermocline water, Wiley Online Library, 1986.
- 731 Gordon, A. L., Visbeck, M. and Huber, B.: Export of Weddell Sea deep and bottom water, Wiley Online Library, 2001.
- 732 Griffies, S. M., Biastoch, A., Böning, C., Bryan, F., Danabasoglu, G., Chassignet, E. P., England, M. H., Gerdes, R., Haak,  
733 H. and Hallberg, R. W.: Coordinated ocean-ice reference experiments (COREs), Elsevier, 2009.
- 734 Harrison, L. C., Holland, P. R., Heywood, K. J., Nicholls, K. W. and Brisbourne, A. M.: Sensitivity of melting, freezing and  
735 marine ice beneath Larsen C Ice Shelf to changes in ocean forcing, Wiley Online Library, 2022.
- 736 Hausmann, U., Sallée, J., Jourdain, N. C., Mathiot, P., Rousset, C., Madec, G., Deshayes, J. and Hattermann, T.: The Role of  
737 Tides in Ocean-Ice Shelf Interactions in the Southwestern Weddell Sea, Wiley Online Library, 2020.
- 738 Hazeleger, W., Severijns, C., Semmler, T., Ștefănescu, S., Yang, S., Wang, X., Wyser, K., Dutra, E., Baldasano, J. M. and  
739 Bintanja, R.: EC-Earth: a seamless earth-system prediction approach in action, American Meteorological Society, 2010.
- 740 Hellmer, H. H. and Olbers, D. J.: A two-dimensional model for the thermohaline circulation under an ice shelf, Cambridge  
741 University Press, 1989.
- 742 Hellmer, H. H. : Impact of Antarctic ice shelf basal melting on sea ice and deep ocean properties, Wiley Online Library,  
743 2004.
- 744 Heuzé, C., Heywood, K. J., Stevens, D. P. and Ridley, J. K.: Southern Ocean bottom water characteristics in CMIP5 models,  
745 Wiley Online Library, 2013.
- 746 Heuzé, C. : Antarctic bottom water and North Atlantic deep water in cmip6 models, Copernicus GmbH, 2021.
- 747 Hewitt, H. T., Copsey, D., Culverwell, I. D., Harris, C. M., Hill, R., Keen, A. B., McLaren, A. J. and Hunke, E. C.: Design  
748 and implementation of the infrastructure of HadGEM3: The next-generation Met Office climate modelling system,  
749 Copernicus GmbH, 2011.
- 750 Hewitt, H. T., Roberts, M. J., Hyder, P., Graham, T., Rae, J., Belcher, S. E., Bourdallé-Badie, R., Copsey, D., Coward, A.  
751 and Guiavarch, C.: The impact of resolving the Rossby radius at mid-latitudes in the ocean: Results from a high-resolution  
752 version of the Met Office GC2 coupled model, Copernicus GmbH, 2016.
- 753 Holland, D. M. and Jenkins, A.: Modeling thermodynamic ice–ocean interactions at the base of an ice shelf, 1999.
- 754 Huot, P., Fichet, T., Jourdain, N. C., Mathiot, P., Rousset, C., Kittel, C. and Fettweis, X.: Influence of ocean tides and ice  
755 shelves on ocean–ice interactions and dense shelf water formation in the D’Urville Sea, Antarctica, Elsevier, 2021.
- 756 Hutchinson, K., Deshayes, J., Sallée, J., Dowdeswell, J. A., de Lavergne, C., Anson, I., Luyt, H., Henry, T. and Fawcett, S.  
757 E.: Water mass characteristics and distribution adjacent to Larsen C Ice Shelf, Antarctica, Wiley Online Library, 2020.





- 758 Huthnance, J. M. : Circulation, exchange and water masses at the ocean margin: the role of physical processes at the shelf  
759 edge, Elsevier, 1995.
- 760 Jacobs, S. S., Gordon, A. L. and Ardaí, J. L., Jr: Circulation and melting beneath the ross ice shelf, 203/4379/439 [pii], 1979.
- 761 Janout, M. A., Hellmer, H. H., Hattermann, T., Huhn, O., Sültenfuss, J., Østerhus, S., Stulic, L., Ryan, S., Schröder, M. and  
762 Kanzow, T.: FRIS revisited in 2018: On the circulation and water masses at the Filchner and Ronne ice shelves in the  
763 southern Weddell Sea, Wiley Online Library, 2021.
- 764 Jeong, H., Asay-Davis, X. S., Turner, A. K., Comeau, D. S., Price, S. F., Abernathy, R. P., Veneziani, M., Petersen, M. R.,  
765 Hoffman, M. J. and Mazloff, M. R.: Impacts of ice-shelf melting on water-mass transformation in the Southern Ocean from  
766 E3SM simulations, 2020.
- 767 Johnson, G. C. : Quantifying Antarctic bottom water and North Atlantic deep water volumes, Wiley Online Library, 2008.
- 768 Jourdain, N. C., Mathiot, P., Merino, N., Durand, G., Le Sommer, J., Spence, P., Dutrieux, P. and Madec, G.: Ocean  
769 circulation and sea-ice thinning induced by melting ice shelves in the Amundsen Sea, Wiley Online Library, 2017.
- 770 Kerr, R., Dotto, T. S., Mata, M. M. and Hellmer, H. H.: Three decades of deep water mass investigation in the Weddell Sea  
771 (1984–2014): temporal variability and changes, Elsevier, 2018.
- 772 Killworth, P. D. : Deep convection in the world ocean, Wiley Online Library, 1983.
- 773 Kimmritz, M., Danilov, S. and Losch, M.: The adaptive EVP method for solving the sea ice momentum equation, Elsevier,  
774 2016.
- 775 Large, W. G. and Yeager, S. G.: Diurnal to decadal global forcing for ocean and sea-ice models: the data sets and flux  
776 climatologies. CGD Division of the National Center for Atmospheric Research, NCAR Technical Note: NCAR/TN-  
777 460+STR. Citeseer, 2004.
- 778 Lipscomb, W. H. : Remapping the thickness distribution in sea ice models, Wiley Online Library, 2001.
- 779 Locarnini, M. M., Mishonov, A. V., Baranova, O. K., Boyer, T. P., Zweng, M. M., Garcia, H. E., Seidov, D., Weathers, K.,  
780 Paver, C. and Smolyar, I.: World ocean atlas 2018, volume 1: Temperature, 2018.
- 781 Locarnini, M. M., Mishonov, A. V., Baranova, O. K., Boyer, T. P., Zweng, M. M., Garcia, H. E., Seidov, D., Weathers, K.,  
782 Paver, C. and Smolyar, I.: World ocean atlas 2018, volume 1: Temperature, 2018.
- 783 Locarnini, R. A., A. V. Mishonov, J. I. Antonov, T. P. Boyer, H. E. Garcia, O. K. Baranova, M. M. Zweng, C. R. Paver, J. R.  
784 Reagan, D. R. Johnson, M. Hamilton, and D. Seidov. : World Ocean Atlas 2013, 2013.
- 785 Losch, M. : Modeling ice shelf cavities in a z coordinate ocean general circulation model, Wiley Online Library, 2008.
- 786 Madec, G. and NEMO System Team: Nemo Ocean Engine, 10.5281/zenodo.3878122, 2019.
- 787 Madec, G. and NEMO System Team: NEMO Ocean Engine, 2016.
- 788 Marshall, J. and Speer, K.: Closure of the meridional overturning circulation through Southern Ocean upwelling, Nature  
789 Publishing Group, 2012.
- 790 Mathiot, P., Goosse, H., Fichet, T., Barnier, B. and Gallée, H.: Modelling the seasonal variability of the Antarctic Slope  
791 Current, Copernicus GmbH, 2011.



- 792 **Mathiot, P., Jenkins, A., Harris, C. and Madec, G.: Explicit representation and parametrised**  
793 **impacts of under ice shelf seas in the z\* coordinate ocean model NEMO 3.6, Copernicus**  
794 **GmbH, 2017.**
- 795 Mazloff, M. R., Heimbach, P. and Wunsch, C.: An eddy-permitting Southern Ocean state estimate, American Meteorological  
796 Society, 2010.
- 797 Melsheimer, C. and Spreen, G.: AMSR-E ASI sea ice concentration data, Antarctic, version 5.4 (NetCDF) (June 2002 -  
798 September 2011), <https://doi.pangaea.de/10.1594/PANGAEA.919778>, 2020.
- 799 Menviel, L., Timmermann, A., Timm, O. E. and Mouchet, A.: Climate and biogeochemical response to a rapid melting of  
800 the West Antarctic Ice Sheet during interglacials and implications for future climate, Wiley Online Library, 2010.
- 801 Meredith, M., Sommerkorn, M., Cassotta, S., Derksen, C., Ekaykin, A., Hollowed, A., Kofinas, G., Mackintosh, A.,  
802 Melbourne-Thomas, J., Muelbert, M.M.C. and Ottersen, G. : Polar regions. IPCC Special Report on the Ocean and  
803 Cryosphere in a Changing Climate, <https://www.ipcc.ch/srocc/chapter>, p.2., 2019.
- 804 Merino, N., Le Sommer, J., Durand, G., Jourdain, N. C., Madec, G., Mathiot, P. and Tournadre, J.: Antarctic icebergs melt  
805 over the Southern Ocean: Climatology and impact on sea ice, Elsevier, 2016.
- 806 Moholdt, G., Padman, L. and Fricker, H. A.: Basal mass budget of Ross and Filchner-Ronne ice shelves, Antarctica, derived  
807 from Lagrangian analysis of ICESat altimetry, Wiley Online Library, 2014.
- 808 Mohrmann, M., Heuzé, C. and Swart, S.: Southern Ocean polynyas in CMIP6 models, Copernicus GmbH, 2021.
- 809 Nakayama, Y., Timmermann, R. and Hellmer, H.: Impact of West Antarctic ice shelf melting on Southern Ocean  
810 hydrography, Copernicus GmbH, 2020.
- 811 Naughten, K. A., Meissner, K. J., Galton-Fenzi, B. K., England, M. H., Timmermann, R., Hellmer, H. H., Hattermann, T.  
812 and Debernard, J. B.: Intercomparison of Antarctic ice-shelf, ocean, and sea-ice interactions simulated by MetROMS-  
813 iceshelf and FESOM 1.4, Copernicus GmbH, 2018.
- 814 Naughten, K. A., De Rydt, J., Rosier, S. H., Jenkins, A., Holland, P. R. and Ridley, J. K.: Two-timescale response of a large  
815 Antarctic ice shelf to climate change, Nature Publishing Group, 2021.
- 816 Naveira Garabato, A. C., McDonagh, E. L., Stevens, D. P., Heywood, K. J. and Sanders, R. J.: On the export of Antarctic  
817 bottom water from the Weddell Sea, Elsevier, 2002.
- 818 NEMO System Team. : NEMO ocean engine, scientific notes of climate modelling center, 27, ISSN 1288-1619 Institut  
819 Pierre-Simon Laplace (IPSL), Institut Pierre-Simon Laplace (IPSL), Paris, 10.5281/zenodo.1464816, 2022.
- 820 Nicholls, K. W., Østerhus, S., Makinson, K. and Johnson, M. R.: Oceanographic conditions south of Berkner Island, beneath  
821 Filchner-Ronne Ice Shelf, Antarctica, Wiley Online Library, 2001.
- 822 Nicholls, K. W., Pudsey, C. J. and Morris, P.: Summertime water masses off the northern Larsen C Ice Shelf, Antarctica,  
823 Wiley Online Library, 2004.
- 824 Nicholls, K. W., Østerhus, S., Makinson, K., Gammelsrød, T. and Fahrbach, E.: Ice-ocean processes over the continental  
825 shelf of the southern Weddell Sea, Antarctica: A review, Wiley Online Library, 2009.
- 826 NOAA. : National Geophysical Data Center 2-minute gridded global relief data (ETOPO2) v2, 2006.
- 827 Orsi, A. H., Johnson, G. C. and Bullister, J. L.: Circulation, mixing, and production of Antarctic Bottom Water, Elsevier,  
828 1999.



- 829 Orsi, A. H. : Recycling bottom waters, Nature Publishing Group, 2010.
- 830 Phipps, S. J., Fogwill, C. J. and Turney, C. S.: Impacts of marine instability across the East Antarctic Ice Sheet on Southern  
831 Ocean dynamics, Copernicus GmbH, 2016.
- 832 Prather, M. J. : Numerical advection by conservation of second-order moments, Wiley Online Library, 1986.
- 833 Rignot, E., Jacobs, S., Mouginot, J. and Scheuchl, B.: Ice-shelf melting around Antarctica, American Association for the  
834 Advancement of Science, 2013.
- 835 Rintoul, S. R. : The global influence of localized dynamics in the Southern Ocean, Nature Publishing Group, 2018.
- 836 Robertson, R., Visbeck, M., Gordon, A. L. and Fahrbach, E.: Long-term temperature trends in the deep waters of the  
837 Weddell Sea, Elsevier, 2002.
- 838 Rohardt, G., Fahrbach, E., Beszczynska-Möller, A., Boetius, A., Brunßen, J., Budéus, G., Cisewski, B., Engbrodt, R.,  
839 Gauger, S., Geibert, W., Geprägs, P., Gerdes, D., Gersonde, R., Gordon, A. L., Hellmer, H. H., Isla, E., Jacobs, S. S., Janout,  
840 M. A., Jokat, W., Klages, M., Kuhn, G., Meincke, J., Ober, S., Østerhus, S., Peterson, R. G., Rabe, B., Rudels, B., Schauer,  
841 U., Schröder, M., Sildam, J., Soltwedel, T., Stangeew, E., Stein, M., Strass, V. H., Thiede, J., Tippenhauer, S., Veth, C., von  
842 Appen, W., Weirig, M., Wisotzki, A., Wolf-Gladrow, D. A. and Kanzow, T.: Physical oceanography on board of  
843 POLARSTERN (1983-11-22 to 2016-02-14). Alfred Wegener Institute, Helmholtz Centre for Polar and Marine Research,  
844 Bremerhaven, 10.1594/PANGAEA.860066, 2016.
- 845 Sallée, J., Pellichero, V., Akhoudas, C., Pauthenet, E., Vignes, L., Schmidtko, S., Garabato, A. N., Sutherland, P. and  
846 Kuusela, M.: Summertime increases in upper-ocean stratification and mixed-layer depth, Nature Publishing Group, 2021.
- 847 Scoccimarro, E., Gualdi, S., Bellucci, A., Sanna, A., Giuseppe Fogli, P., Manzini, E., Vichi, M., Oddo, P. and Navarra, A.:  
848 Effects of tropical cyclones on ocean heat transport in a high-resolution coupled general circulation model, 2011.
- 849 Siahhaan, A., Smith, R., Holland, P., Jenkins, A., Gregory, J. M., Lee, V., Mathiot, P., Payne, T., Ridley, J. and Jones, C.: The  
850 Antarctic contribution to 21st century sea-level rise predicted by the UK Earth System Model with an interactive ice sheet,  
851 Copernicus GmbH, 2021.
- 852 Smethie Jr, W. M. and Jacobs, S. S.: Circulation and melting under the Ross Ice Shelf: estimates from evolving CFC, salinity  
853 and temperature fields in the Ross Sea, Elsevier, 2005.
- 854 Smith, R. S., Mathiot, P., Siahhaan, A., Lee, V., Cornford, S. L., Gregory, J. M., Payne, A. J., Jenkins, A., Holland, P. R. and  
855 Ridley, J. K.: Coupling the UK Earth System Model to dynamic models of the Greenland and Antarctic ice sheets, Wiley  
856 Online Library, 2021.
- 857 Solodoch, A., Stewart, A. L., Hogg, A. M., Morrison, A. K., Kiss, A. E., Thompson, A. F., Purkey, S. G. and Cimoli, L.:  
858 How Does Antarctic Bottom Water Cross the Southern Ocean? Wiley Online Library, 2022.
- 859 Solodoch, A., Stewart, A. L., Hogg, A. M., Morrison, A. K., Kiss, A. E., Thompson, A. F., Purkey, S. G. and Cimoli, L.:  
860 How Does Antarctic Bottom Water Cross the Southern Ocean? Wiley Online Library, 2022.
- 861 Storkey, D., Blaker, A. T., Mathiot, P., Megann, A., Aksenov, Y., Blockley, E. W., Calvert, D., Graham, T., Hewitt, H. T.  
862 and Hyder, P.: UK Global Ocean GO6 and GO7: A traceable hierarchy of model resolutions, Copernicus GmbH, 2018.
- 863 Swart, N. C., Cole, J. N., Kharin, V. V., Lazare, M., Scinocca, J. F., Gillett, N. P., Anstey, J., Arora, V., Christian, J. R. and  
864 Hanna, S.: The Canadian earth system model version 5 (CanESM5. 0.3), Copernicus GmbH, 2019.
- 865 Thompson, A. F., Stewart, A. L., Spence, P. and Heywood, K. J.: The Antarctic Slope Current in a changing climate, Wiley  
866 Online Library, 2018.



- 867 Vancoppenolle, M., Rousset, C., Blockley, E., and the NEMO Sea Ice Working Group: SI3 – Sea Ice modelling Integrated  
868 Initiative – The NEMO Sea Ice Engine, 10.5281/zenodo.7534900, 2023.
- 869 Van Caspel, M., Schröder, M., Huhn, O. and Hellmer, H. H.: Precursors of Antarctic Bottom Water formed on the  
870 continental shelf off Larsen Ice Shelf, Elsevier, 2015.
- 871 Voltaire, A., Sanchez-Gomez, E., Salas y Méliá, D., Decharme, B., Cassou, C., Sénési, S., Valcke, S., Beau, I., Alias, A. and  
872 Chevallier, M.: The CNRM-CM5. 1 global climate model: description and basic evaluation, Springer, 2013.
- 873 Whitehead, J. A. : Dense water off continents, Nature Publishing Group, 1987.
- 874 Zweng, M. M., Seidov, D., Boyer, T. P., Locarnini, M., Garcia, H. E., Mishonov, A. V., Baranova, O. K., Weathers, K.,  
875 Paver, C. R. and Smolyar, I.: World ocean atlas 2018, volume 2: Salinity, 2019.
- 876 Zweng, M.M, J.R. Reagan, J.I. Antonov, R.A. Locarnini, A.V. Mishonov, T.P. Boyer, H.E. Garcia, O.K. Baranova, D.R.  
877 Johnson, D.Seidov, M.M. Biddle. : World Ocean Atlas 2013, 2013.
- 878
- 879
- 880
- 881
- 882
- 883
- 884
- 885
- 886
- 887
- 888
- 889
- 890
- 891
- 892
- 893
- 894
- 895
- 896